

LESnets (Large-Eddy Simulation nets): Physics-informed neural operator for large-eddy simulation of turbulence

Sunan Zhao^{a,b,c}, Zhijie Li^{a,d}, Boyu Fan^{a,b,c}, Yunpeng Wang^{a,b,c}, Huiyu Yang^{a,b,c}, Jianchun Wang^{a,b,c,*}

^aDepartment of Mechanics and Aerospace Engineering, Southern University of Science and Technology, Shenzhen, 518055, , China

^bGuangdong Provincial Key Laboratory of Turbulence Research and Applications, Southern University of Science and Technology, Shenzhen, 518055, , China

^cGuangdong-Hong Kong-Macao Joint Laboratory for Data-Driven Fluid Mechanics and Engineering Applications, Southern University of Science and Technology, Shenzhen, 518055, , China

^dDepartment of Biomedical Engineering Applications, National University of Singapore, Singapore, 117583, , Singapore

Abstract

Acquisition of large datasets for three-dimensional (3D) partial differential equations are usually very expensive. Physics-informed neural operator (PINO) eliminates the high costs associated with generation of training datasets, and shows great potential in a variety of partial differential equations. In this work, we employ physics-informed neural operator, encoding the large-eddy simulation (LES) equations directly into the neural operator for simulating three-dimensional incompressible turbulent flows. We develop the LESnets (Large-Eddy Simulation nets) by adding large-eddy simulation equations to two different data-driven models, including Fourier neural operator (FNO) and implicit Fourier neural operator (IFNO) without using label data. Notably, by leveraging only PDE constraints to learn the spatio-temporal dynamics problem, LESnets retains the computational efficiency of data-driven approaches while obviating the necessity for data. Meanwhile, using large-eddy simulation equations as PDE constraints makes it possible to efficiently predict complex turbulence at coarse grids. We investigate the performance of the LESnets with two standard three-dimensional turbulent flows: decaying homogeneous isotropic turbulence and temporally evolving turbulent mixing layer. In the numerical experiments, the LESnets model shows a similar or even better accuracy as compared to traditional large-eddy simulation and data-driven models of FNO and IFNO. Moreover, the well-trained LESnets is significantly faster than traditional LES, and has a similar efficiency as the data-driven FNO and IFNO models. Thus, physics-informed neural operators have a strong potential for 3D nonlinear engineering applications.

Keywords:

Fourier neural operator

Physics-informed neural operator

Turbulence

Large-eddy simulation

1. Introduction

Over the past few decades, the computational fluid dynamics (CFD) methods have a variety of applications in aerospace engineering and industrial production [108]. Multi-scale structures of turbulent flows can result in significant computational time. Thus, Reynolds-Averaged Navier-Stokes simulation (RANS) [66] method and Large-Eddy Simulation (LES) [107] method are used for turbulence simulation to reduce the computational costs. In the past decade, neural networks (NNs) have been applied to develop advanced turbulence models and simulation methods [2, 11, 18, 22–27, 104, 105]. Most of the early approaches use machine learning (ML) to develop accurate turbulence

*Corresponding author at: Department of Mechanics and Aerospace Engineering, Southern University of Science and Technology, Shenzhen 518055, China.

E-mail address: wangjc@sustech.edu.cn (J. Wang).

models for RANS and LES [32–35, 48–50]. Ling et al. [49] proposed a novel neural network which uses multiplicative layer with an invariant tensor basis to embed Galilean invariance into the predicted anisotropic component of Reynolds stress, and demonstrated a better accuracy for predicting the Reynolds stress tensor. Wu et al. [103] proposed a metric based on local condition number for *a priori* evaluation of the conditioning of the RANS equations, which serves as a guide for subsequent data-driven RANS model. Beck et al. [102] proposed convolutional neural networks (CNNs) and residual neural networks (RNNs) to construct accurate subgrid-scale (SGS) models for LES. Park et al. and Wang et al. [47, 101] also applied NNs to learn accurate closures of SGS stress in LES of turbulence.

Many recent studies have focused on approximating the Navier–Stokes equations using deep neural networks [98, 99]. Raissi et al. [95–97] introduced the physics-informed neural networks (PINNs) to solve forward and inverse problems of partial differential equations (PDEs). Subsequently, this approach [44, 45] has also been used to address the missing flow dynamics [94] and simulate vortex induced vibrations [93]. PINNs are free of large training data and complicated grids, and demonstrate a great potential in solving various partial differential equations. However, PINNs have the problem of tuning of weight hyperparameters for the physics-informed term, the data-mismatch term of the loss function, and the convergence problem for complex parameter functions [16, 120]. In order to alleviate the above problems, many improvement methods have been developed [1, 14, 31, 89–92] and applied to the task of turbulence prediction [13, 30, 51, 67]. However, most of the relevant studies focus on ordinary differential equations (ODEs) or 2D simple PDEs. Learning with PINNs for three-dimensional complex PDEs, e.g 3D Navier–Stokes (NS) equations, is a challenging problem. Jin et al. [115] developed the Navier–Stokes flow nets (NSFnets) by embedding the governing equations, initial conditions, and boundary conditions into the loss function to simulate three-dimensional turbulent channel flow. Recently, Cai et al. [38] proposed a new method based on physics-informed neural networks (PINNs) to infer the full continuous velocity and pressure fields from snapshots of 3-D temperature fields obtained by TomoBOS imaging. Zhu et al. [39] developed a physics-informed neural network to significantly augment state-of-the-art experimental data of 3D stratified flows. Chen et al. [88] used a multi-scale version of physics-informed neural network for 3D wind field reconstruction from LiDAR measurements. Cai et al. [46] applied PINNs to reconstruct the 3D wake flow fields based on a few two-dimensional and two-component (2D2C) velocity observations.

Operator learning serves as another paradigm for solving PDE with machine learning [6, 15, 17, 19, 28, 42, 43]. By learning a map between the input condition and the PDE solution in a data-driven manner, neural operators manage to solve a family of PDEs [87]. Deep operator network (DeepOnet) and Fourier neural operator (FNO) are two of most popular operator learning methods. A DeepONet consists of two sub-networks, one for encoding the input function (branch net), and another for encoding the locations (trunk net) [15]. The main idea of FNO is to use Fourier transform to map high-dimensional data into the frequency domain and approximate nonlinear operators by learning the relationships between Fourier coefficients through neural networks [116]. The FNO model outperforms the state-of-the-art models, including U-Net [86] TF-Net [85] and ResNet [84] in two-dimensional (2D) turbulence prediction. You et al. [118] developed an implicit Fourier neural operator (IFNO), to model the increment between layers as an integral operator to capture the long-range dependencies in the feature space. The developments and applications of FNO based models have been increasing [20, 21, 69, 70, 80–83]. However, the majority of the works have been focused on one-dimensional (1D) and two dimensional (2D) problems. Utilizing deep neural networks to model 3D turbulence poses a more significant challenge due to the substantial growth in both size and dimension of simulation data [79]. Recently, Peng et al. [78] added attention mechanisms to FNO to predict three-dimensional turbulence. Li et al. and Wang et al. [77, 121] developed an implicit U-Net enhanced FNO (IUFNO) using the coarse-grid filtered DNS (fDNS) data for fast prediction of 3D isotropic turbulence, a turbulent mixing layer and turbulent channel flows. Large dataset of coarse grid filtered DNS were used for training IUFNO models. Although the well-trained operator learning models are accurate and effective in the aforementioned problems, they still lack interpretability of physics and rely on high-resolution training data.

In recent research, the physics-informed approach has been applied to operator learning by embedding PDEs into the loss functions in a manner similar to PINNs, including physics-informed DeepONets [76, 122, 123], physics-informed Fourier neural operator [3, 7, 9, 12, 111, 120] and physics-informed transformer [4, 10, 40]. Physics-informed neural operator (PINO) models have proven to produce very accurate results in several typical linear and non-linear PDE settings [8, 29, 68, 71–75]. Nevertheless, for high-dimensional complex partial differential equations, the generalization capability, the computational efficiency, and the optimization of the physics-informed neural operator models will encounter significant challenges. In the present study, we propose Large-Eddy Simulation nets (LESnets) by embedding large-eddy simulation equations to two neural operator models (FNO and IFNO) to predict the 3D

turbulence. The proposed LESnets aims to effectively simulate turbulent flows without training data and maintain the efficiency of data-driven neural operators.

The rest of the paper is organized as follows. In Section 2, governing equations of the large-eddy simulation, and LESnets and architectures of PINNs, FNO, PINO are presented. We then present LESnets results for decaying homogeneous isotropic turbulence and temporally evolving turbulent mixing layer, and compare computational efficiency of LESnets with traditional large-eddy simulation methods and data-driven methods in Section 3. We summarize our results in Section 4.

2. Methodology

2.1. Governing equations

The 3D incompressible turbulent flows of Newtonian fluid are governed by the 3D Navier-Stokes (NS) equations, namely [106, 108]

$$\frac{\partial u_i}{\partial x_i} = 0, \quad (1)$$

$$\frac{\partial u_i}{\partial t} + \frac{\partial u_i u_j}{\partial x_j} = -\frac{\partial p}{\partial x_i} + \nu \frac{\partial^2 u_i}{\partial x_j \partial x_j} + \mathcal{F}_i, \quad (2)$$

where t is time, u_i denotes the i th component of velocity, p is the pressure divided by the constant density, ν represents the kinematic viscosity, and \mathcal{F}_i stands for a large-scale forcing to the momentum of the fluid in the i th coordinate direction. In this paper, the convention of summation notation is employed.

Even though the NS equations were discovered more than a century ago, seeking the full-scale solutions of these equations using DNS is still impractical at high Reynolds numbers [64, 65]. Unlike DNS, LES only solves the major energy-containing large-scale motions using a coarse grid, leaving the effects of subgrid motions handled by the subgrid scale (SGS) models [62, 110]. The filtered incompressible Navier–Stokes equations can be derived for the resolved fields as follows: [63, 108]

$$\frac{\partial \bar{u}_i}{\partial x_i} = 0, \quad (3)$$

$$\frac{\partial \bar{u}_i}{\partial t} + \frac{\partial \bar{u}_i \bar{u}_j}{\partial x_j} = -\frac{\partial \bar{p}}{\partial x_i} - \frac{\partial \tau_{ij}}{\partial x_j} + \nu \frac{\partial^2 \bar{u}_i}{\partial x_j \partial x_j} + \bar{\mathcal{F}}_i, \quad (4)$$

where \bar{u} represents the coarse-grid filtered DNS (fDNS) velocity, and τ_{ij} is the unclosed sub-grid scale (SGS) stress defined by $\tau_{ij} = \overline{u_i u_j} - \bar{u}_i \bar{u}_j$. In order to solve the LES equations, it is crucial to model the SGS stress as a function of the filtered variables. A very well-known SGS model is the Smagorinsky model (SM) [110], which can be written as

$$\tau_{ij}^A = \tau_{ij} - \frac{\delta_{ij}}{3} \tau_{kk} = -2C_{\text{Smag}}^2 \bar{\Delta}^2 |\bar{S}| \bar{S}_{ij}, \quad (5)$$

where δ_{ij} represents Kronecker symbol, C_{Smag} is the Smagorinsky coefficient, $\bar{\Delta}$ is the filter width and \bar{S}_{ij} is the filtered strain rate. $|\bar{S}| = \sqrt{2\bar{S}_{ij}\bar{S}_{ij}}$ is the characteristic filtered strain rate.

The integral length scale L_I and the large-eddy turnover time τ are respectively given by

$$L_I = \frac{3\pi}{2(u^{rms})^2} \int_0^\infty \frac{E(k)}{k} dk, \quad \tau = \frac{L_I}{u^{rms}}, \quad (6)$$

where $u^{rms} = \sqrt{\langle u_i u_i \rangle}$ is the root mean square (rms) of the velocity, and $E(k)$ is the energy spectrum.

In this study, we choose LES equations Eq.(3) and Eq.(4) along with the Smagorinsky model as equation constraints. We investigate the possibility of using physics-informed neural operator (PINO) to learn the solution operator, and compare the PINO with conventional LES models, PINNs and data-driven neural operators.

2.2. Physics-informed neural networks (PINNs)

Let's consider a general form of the dynamical system governing by the following PDE

$$\begin{aligned}\frac{\partial u}{\partial t} &= \mathcal{R}(u), & \text{in } D \times (0, \infty), \\ u &= g, & \text{in } \partial D \times (0, \infty), \\ u &= a, & \text{in } D \times \{0\},\end{aligned}\tag{7}$$

where D is a bounded domain, ∂D is a Dirichlet boundary, $a(x) = u(x, 0) \in \mathcal{A} \subseteq \mathcal{V}$ is the initial condition, $u(x, t) \in \mathcal{U}$ for $t > 0$ is the unknown, and \mathcal{R} is a non-linear partial differential operator with \mathcal{U} and \mathcal{V} being Banach spaces. Here, $g(x, t)$ is a known boundary condition. We assume that u is bounded for all time and for every $u(x, 0) \in \mathcal{A}$.

This formulation gives rise to the solution operator $\mathcal{G}^\dagger : \mathcal{A} \rightarrow C((0, T]; \mathcal{U})$ defined by $a \mapsto u$. Given an instance a and a solution operator \mathcal{G}^\dagger defined by Eq.(7), we denote $u^\dagger = \mathcal{G}^\dagger(a)$ as the unique ground truth [111]. The equation solving task is to approximate u^\dagger .

The PINN-type methods use a neural network u_θ with parameters θ as the ansatz to approximate the solution function u^\dagger . The parameters θ are obtained by minimizing the physics-informed loss with exact derivatives computed using automatic-differentiation (autograd) [112].

A typical choice for physics-informed loss is the $L^2((0, T]; L^2(D))$ norm, yielding [97]

$$\begin{aligned}\mathcal{L}_{\text{pde}}(a, u_\theta) &= \left\| \frac{du_\theta}{dt} - \mathcal{R}(u_\theta) \right\|_{L^2(D; T)}^2 + \alpha \|u_\theta|_{\partial D} - g\|_{L^2(\partial D; T)}^2 + \beta \|u_\theta|_{t=0} - a\|_{L^2(D)}^2 \\ &= \int_0^T \int_D \left| \frac{du_\theta}{dt}(x, t) - \mathcal{R}(u_\theta)(x, t) \right|^2 dx dt \\ &\quad + \alpha \int_0^T \int_{\partial D} |u_\theta(x, t) - g(x, t)|^2 dx dt \\ &\quad + \beta \int_D |u_\theta(0, x) - a(x)|^2 dx.\end{aligned}\tag{8}$$

The PDE loss consists of the physics loss in the interior and the loss on the boundary and initial conditions, with hyper-parameters $\alpha, \beta > 0$.

However, PINNs often fail to solve challenging PDEs when the solution exhibits high-frequency or multi-scale structure [113, 114]. In multi-scale problems such as three-dimensional turbulence, the present PINNs is only able to solve the PDE in a small spatial domain or for a limited time domain [115]. Alternatively, additional observational data are required as a supplement to PINN, which is not always feasible in practical applications [37, 46].

2.3. Neural operator

In general, the neural operators can approximate the operator in Eq.(7) which is a non-linear mapping between infinite-dimensional spaces [87]

$$G : a = u(x, 0) \in \mathcal{A} \times \Theta \mapsto u(x, t) \in \mathcal{U},\tag{9}$$

where $\mathcal{A} = \mathcal{A}(D; \mathbb{R}^{d_a})$ and $\mathcal{U} = \mathcal{U}(D; \mathbb{R}^{d_u})$ are separable Banach spaces of function taking values in \mathbb{R}^{d_a} and \mathbb{R}^{d_u} respectively, and $D \subset \mathbb{R}^d$ is a bounded, open set. For some finite-dimensional parameter space Θ by choosing $\theta^\dagger \in \Theta$ so that $\mathcal{G}(\cdot, \theta^\dagger) = \mathcal{G}_\theta \approx \mathcal{G}^\dagger$. This mapping provides the operator with the advantages of resolution-invariant. There exist numerous effective operator learning models that have demonstrated outstanding performance across a wide range of problems [120, 121]. One can use a neural operator \mathcal{G}_θ with parameters θ as a surrogate model to approximate \mathcal{G}^\dagger . Using an existing dataset $\{a_j, u_j\}_{j=1}^N$ as a ground truth, we can minimize the empirical error on a given pair of data

$$\mathcal{L}_{\text{data}}(u, \mathcal{G}_\theta(a)) = \|u - \mathcal{G}_\theta(a)\|_{\mathcal{U}}^2 = \int_D |u(x) - \mathcal{G}_\theta(a)(x)|^2 dx.\tag{10}$$

The neural operator can be formulated as an iterative architecture $v_0 \mapsto v_1 \cdots \mapsto v_T$, where v_j for $j = 0, 1, \dots, T-1$ is a sequence of functions each taking values in \mathbb{R}^{d_v} [116]. As shown in Fig. 1, the input $a \in \mathcal{A}$ is first lifted to a higher dimension space with the ‘width’ d_v through a fully connected neural network P that is parameterized. Then, through multiple iterations of $v_t \mapsto v_{t+1}$, the output $u(x) = \mathcal{Q}(v_T(x))$ is mapped back to the original physical space using another fully connected neural network layer. The iteration $v_t \mapsto v_{t+1}$ is defined as a combination of a non-local integral operator \mathcal{K} and a local, nonlinear activation function σ . Consequently, the iteration process can be expressed in the following form [116]

$$v_{t+1}(x) := \sigma\left(Wv_t(x) + \left(\mathcal{K}(a; \phi)v_t\right)(x)\right), \quad \forall x \in D, \quad (11)$$

where $\mathcal{K} : \mathcal{A} \times \Theta_{\mathcal{K}} \rightarrow \mathcal{L}(\mathcal{U}(D; \mathbb{R}^{d_v}))$ maps to bounded linear operators on $\mathcal{U}(D; \mathbb{R}^{d_v})$ and is parameterized by $\phi \in \Theta_{\mathcal{K}}$, $W : \mathbb{R}^{d_v} \rightarrow \mathbb{R}^{d_v}$ is a linear transformation. \mathcal{K} is parameterized as a kernel integral transformation by a neural network $\kappa_{\phi} : \mathbb{R}^{2(d+d_a)} \rightarrow \mathbb{R}^{d_v \times d_v}$ parameterized by $\phi \in \Theta_{\mathcal{K}}$. Generally \mathcal{K} is defined as follows:

$$(\mathcal{K}(a; \phi)v_t)(x) := \int_D \kappa(x, y, a(x), a(y); \phi) v_t(y) dy, \quad \forall x \in D. \quad (12)$$

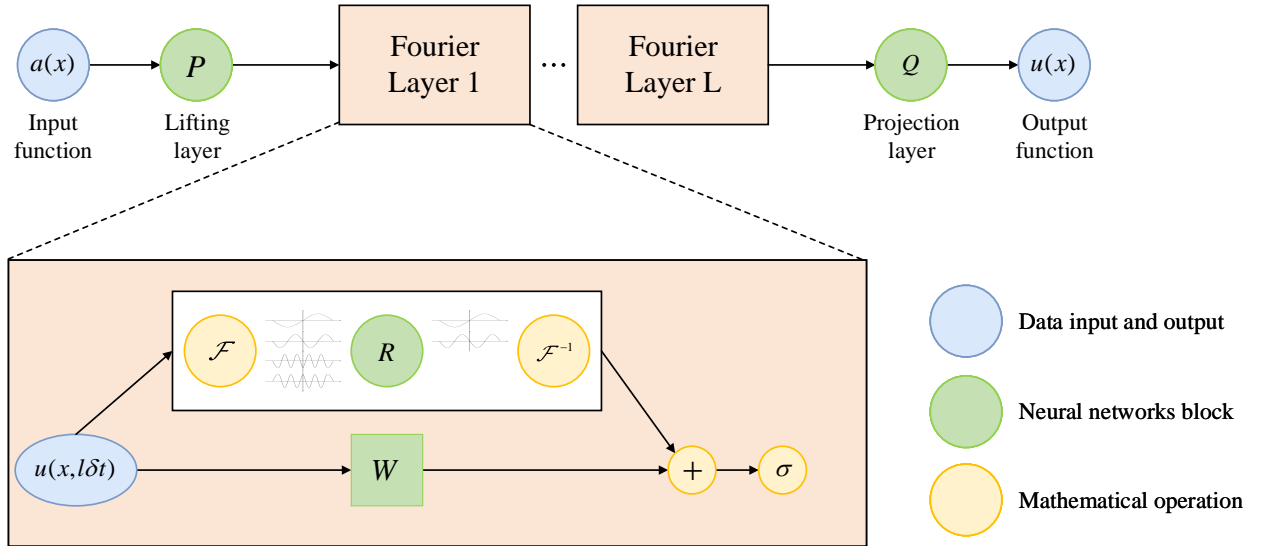


Fig. 1. The architecture of the Fourier neural operator (FNO). The input function, $a(x)$ is transformed to a higher dimension channel space ‘width’ d_v using a fully neural network P and then apply L Fourier layers. Within each Fourier layer, a Fourier transform \mathcal{F} , a linear transform R on the lower Fourier modes and filters out the higher modes; and then converted back to physical space using inverse Fourier transform \mathcal{F}^{-1} . W is a local linear transform. At the end of the Fourier layers, a fully neural network Q is applied to convert the output space to target dimension.

In this work, we employ the Fourier neural operator (FNO) [116] and implicit Fourier neural operator (IFNO) [118] for large-eddy simulation of turbulence. The Fourier neural operator establishes a system with mixed kernel integral and Fourier convolution layers. By mapping the input \mathcal{A} into Fourier space for efficient computation and parameter learning, the Fourier neural operator achieves a very high computational efficiency [116].

FNO parameterizes Eq. (12) in Fourier space. Let \mathcal{F} denotes the Fourier transform of a function $f : D \rightarrow \mathbb{R}^{d_v}$ and \mathcal{F}^{-1} its inverse, then

$$(\mathcal{F}f)_j(k) = \int_D f_j(x) e^{-2i\pi\langle x, k \rangle} dx, \quad (\mathcal{F}^{-1}f)_j(x) = \int_D f_j(k) e^{2i\pi\langle x, k \rangle} dk.$$

The Fourier integral operator \mathcal{K} is given by

$$(\mathcal{K}(\phi)v_t)(x) = \mathcal{F}^{-1}\left(R_{\phi} \cdot (\mathcal{F}v_t)\right)(x), \quad \forall x \in D. \quad (13)$$

By truncating the Fourier series at a specified maximum number of modes $k_{\max} = |\mathbb{Z}_{k_{\max}}| = \{k \in \mathbb{Z}^d : |k_j| \leq k_{\max,j}, \text{ for } j = 1, \dots, d\}$, a finite-dimensional parameterization is achieved. $\mathcal{F}(v_t) \in \mathbb{C}^{n \times d_v}$ can be obtained by discretizing domain D with $n \in \mathbb{N}$ points [116]. R_ϕ is a Fourier transform of a periodic function, which is parameterized as complex-valued-tensor ($k_{\max} \times d_v \times d_v$) containing a collection of truncated Fourier modes $R_\phi \in \mathbb{C}^{k_{\max} \times d_v \times d_v}$. Therefore, the following equation can be derived by multiplying R_ϕ and $\mathcal{F}(v_t)$:

$$(R_\phi \cdot (\mathcal{F}v_t))_{k,l} = \sum_{j=1}^{d_v} R_{\phi k,l,j} (\mathcal{F}v_t)_{k,j}, \quad k = 1, \dots, k_{\max}, \quad j = 1, \dots, d_v. \quad (14)$$

It has been demonstrated that with a large enough value of depth L , FNO can serve as an universal approximator capable of accurately representing any continuous operator [119]. However, with the increasing of Fourier layer L , the increase of parameters makes FNO lose its original efficiency. Subsequently, the proposed implicit Fourier neural operator (IFNO) as shown in Fig. 2 reduces parameters and computational memory by sharing parameters across Fourier layers [118]. The IFNO iteration process can be expressed as follows

$$v_{t+1}(x) := v_t(x) + \delta t \sigma \left(W v_t(x) + \left(\mathcal{K}(a; \phi) v_t \right) (x) \right), \quad \forall x \in D, \quad (15)$$

where δt is the time interval between input and output.

As a form of supervised learning, data-driven operator learning require a substantial amount of high-resolution data. However, in the field of computational fluid dynamics, acquiring such high-resolution fluid data is highly costly and time-consuming, thereby compromising its inherent speed.

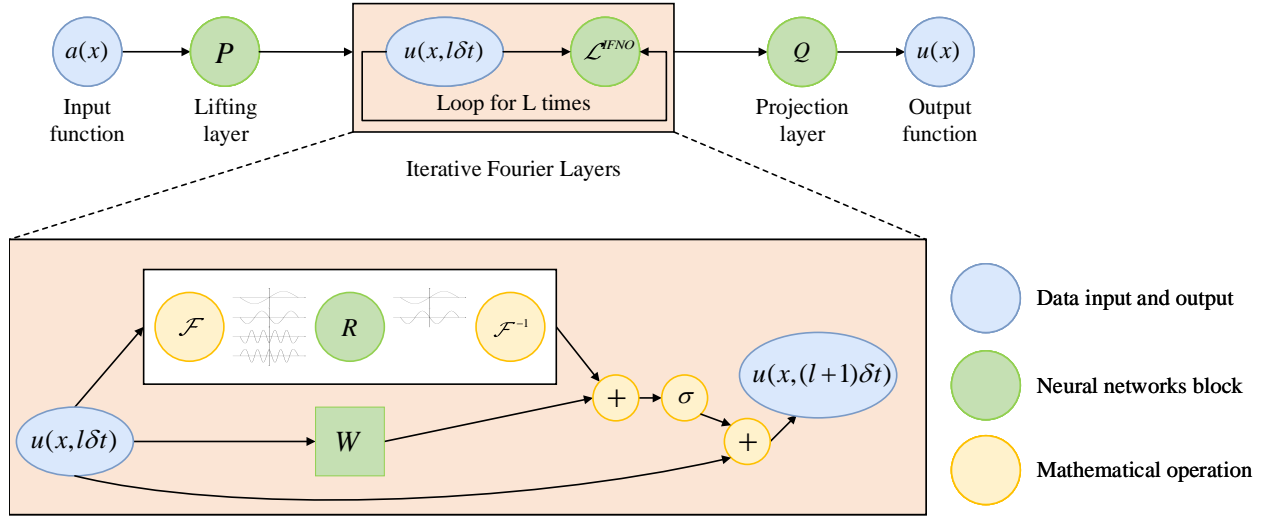


Fig. 2. The architecture of the implicit Fourier neural operator (IFNO).

2.4. Physics-informed neural operator

To combine the respective advantages of PINNs and operator learning, physics-informed neural operator (PINO) [111] has been proposed. By using data loss $\mathcal{L}_{\text{data}}$ Eq.(10) and PDE loss \mathcal{L}_{pde} Eq.(8), the neural operator \mathcal{G}_θ is able to approximate the target solution operator \mathcal{G}^\dagger . Using the PDE constraints of equations makes the neural operator adhere to physical laws, meanwhile, the data loss also facilitates the optimization process.

To fully leverage the advantages of operator learning and save computational time, PINO has developed an efficient and exact derivative computation method similar to automatic differentiation, which calculates full gradient field through the architecture of neural operators. Additionally, by applying the chain rule, derivatives in Fourier space can be directly calculated [111]. The time derivative is calculated using a central difference method as

$$\left\{ \frac{\partial u}{\partial t} \right\}^i = \frac{(u^{i+1} - u^{i-1}))}{2dt}, \quad i = 2, \dots, T-1, \quad (16)$$

where i is the time node, dt is the time interval, and T is the total number of time nodes. For non-periodic problems, the periodic boundary conditions can be recovered by padding the boundaries [111].

The original PINO encounters several significant challenges:

- Based on the standard relative error $L_2 = \|u^* - u\|_2 / \|u\|_2$ of two-dimensional turbulence, the model prediction at short-time ($T = 0.125$) gets 6% error under the constraint of partial differential equations (PDEs), but almost 74% error in the prediction of long time series ($T = 0.5$) [111]. Here, u is the true value, u^* is the predicted value, and $\|\cdot\|_2$ is the L_2 norm.
- It optimizes the equation loss, initial condition loss and data loss concurrently, leading to the challenge for the selection of hyper-parameters for the multitude of losses. Despite attempts to mitigate this issue through adaptive parameters [61], the coexistence of multiple losses complicates the optimization landscape.
- The training and prediction time periods for PINO overlap, implying that PINO is not generalized to subsequent times and does not make predictions over an extended period.

Since initial condition is also a learning target, the original form of PINO is hard to be generalized to other time periods for different initial conditions.

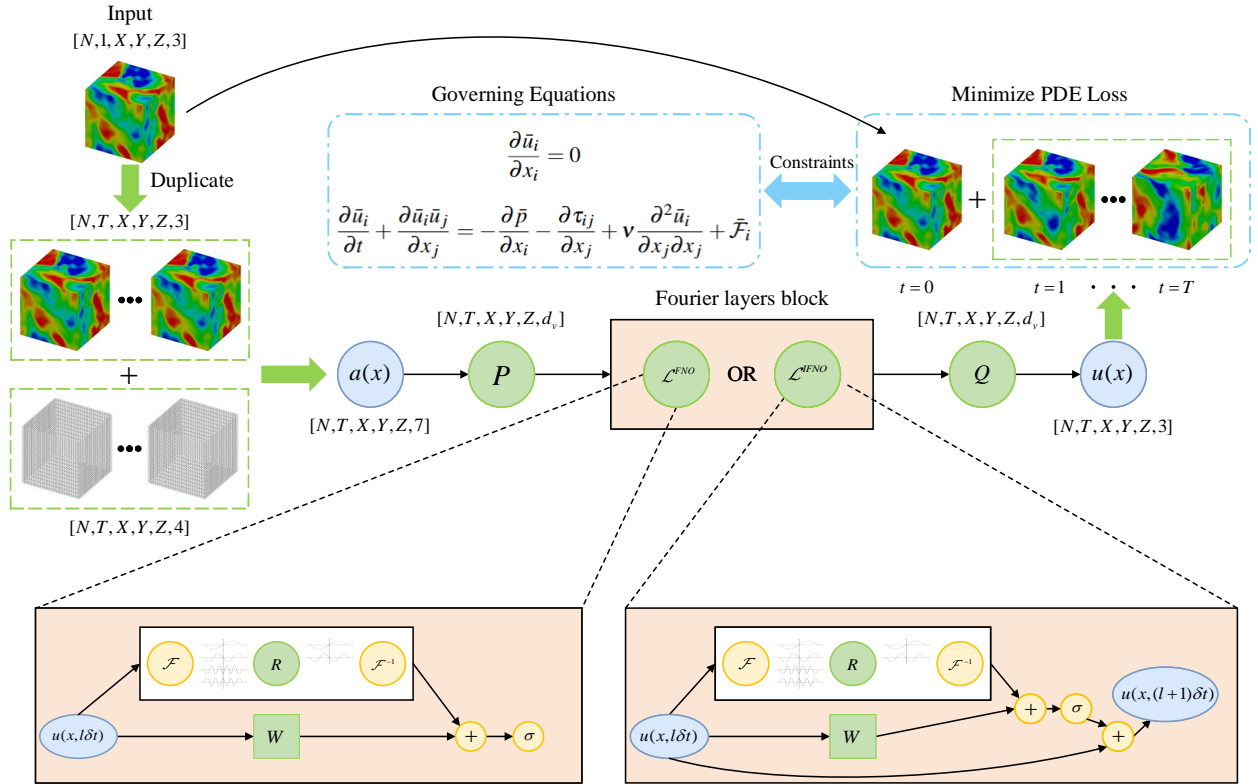


Fig. 3. The architecture of the Large-Eddy Simulation nets (LESnets), using the ideas of physics-informed neural operator to combined the FNO or IFNO model with LES equations constraints.

2.5. LESnets (Large-Eddy Simulation nets)

Based on methods introduced in Sections 2.2 to 2.4, we present LESnets that learns a neural operator \mathcal{G}_θ followed the Eq. (3) and (4) with Smagorinsky model. The schematic of LESnets is illustrated in Fig. 3. The key components of the proposed methods include:

- Employ the neural operator \mathcal{G}_θ via Fourier neural operator (FNO) and implicit Fourier neural operator (IFNO) to verify the effectiveness of our method.
- Utilize the large-eddy simulation equations with a classical SGS model as physical constraints to construct PDE loss for optimizing the operator without any data label.
- Use the initial conditions u_t as known quantities rather than quantities to be learned, and directly combine it with the subsequently output fields $u_{t+1} \cdots u_{t+T}$ to calculate the PDE loss. Additionally, periodic boundary conditions are applied to simplify the optimization process by allowing the LESnets to only consider the PDE loss.
- Train the model with the input-output pair from just one time node: $u_t \mapsto u_{t+1} \cdots u_{t+T}$. In the new prediction, the predicted u_{t+T} is once again input into the model as the initial field to obtain $u_{t+T} \mapsto u_{t+T+1} \cdots u_{t+2T}, \cdots$. Therefore, we only need one initial field u_t for both training and predicting. This closely mimics the traditional CFD approach.

During the training of LESnets, the loss function \mathcal{L}_{PDE} is constructed as follows:

$$\begin{aligned}\mathcal{L}_1 &= \nabla \cdot \bar{u}, \\ \mathcal{L}_2 &= \partial_t \bar{u} + \bar{u} \cdot \nabla \bar{u} + \nabla \bar{p} - \nu \nabla^2 \bar{u} - \nabla \tau, \\ \mathcal{L}_{PDE} &= \|\mathcal{L}_1\|_{L^2(T;D)}^2 + \|\mathcal{L}_2\|_{L^2(T;D)}^2.\end{aligned}\tag{17}$$

Here, \bar{u} represents the coarse-grid filtered DNS (fDNS) velocity and the forcing term $\bar{F}_i = 0$ in the present study. The Algorithm 1 summarizes the training process of LESnets. The training process is briefly summarized as:

- Input the prepared initial field $\{\mathbf{u}(t_n)\}_{n=0}^N$ and add the grid information $\{\mathbf{G}(t_n)\}_{n=0}^N$.
- Output the subsequent field $\{\mathbf{u}(t_n)\}_{n=1,T}^N$ through neural operator \mathcal{G}_θ .
- Calculate the PDE loss \mathcal{L}_{PDE} as the target to optimize the model parameters and select the appropriate model parameters in the prediction stage.

Here, T is the output step of LESnets, N_{ep} is the number of training epochs, λ is the learning rate, and N_{bc} is the batch-size of the LESnets. In the training process, the initial field $a = u(x, y, z, 0)$ is input into the LESnets, and the subsequent fields $u(x, y, z, 1), u(x, y, z, 2), \cdots, u(x, y, z, T)$ are output. The initial field and the subsequent fields are accumulated to obtain a time series field $u(x, y, z, 0), u(x, y, z, 1), \cdots, u(x, y, z, T)$. The PDE loss \mathcal{L}_{PDE} followed by Eq. 17 is the optimization objective to optimize the model parameters. In the prediction tasks, we input the obtained $u(x, y, z, T)$ of the last moment into the trained LESnets again as the initial field, and iteratively advance to achieve a longer prediction.

The merits of LESnets in learning a neural operator includes:

- The efficiency of using only one initial field for training and using spectral method for computing PDE loss.
- The flexibility of output time period T .
- The generalization ability of predicting in unseen regime of fluid fields.

As shown in Fig. 4, in the following sections, we will consider two cases of LES of incompressible turbulence: a 3D decaying homogeneous isotropic turbulence, and a 3D temporally evolving turbulent mixing layer. In Fig. 4, the flow fields are visualized by using contours of velocity w in the Z direction and the Q criterion respectively. The definition of Q is defined as follows [53, 54]

Algorithm 1 Training process of LESnets

```

1: Input:
2:    $\{\mathbf{u}(t_n)\}_{n=0}^N \leftarrow$  Training Data
3:    $\{t_{n=0}\} \leftarrow$  Time stamp
4:    $\mathcal{G}_\theta \leftarrow$  Neural operator
5:    $(N_x, N_y, N_z, N_d, T) \leftarrow (32, 32, 32, 3)$ 
6:    $(N_{ep}, \lambda, N_{bc}) \leftarrow (30000, 1e^{-3}, 1)$ 
7:    $\Theta \leftarrow$  Empty List
8:   for  $j = 1$  to  $N_{ep}$  do
9:      $\{\mathbf{G}(t_n)\}_{n=0}^N \sim \mathbb{U}(N_{bc}, N_x, N_y, N_z, N_d + 1, T) \leftarrow$  Grid information
10:     $\{\mathbf{u}(t_n)\}_{n=0}^N = \{\mathbf{u}(t_n)\}_{n=0}^N + \{\mathbf{G}(t_n)\}_{n=0}^N \leftarrow$  Add at dimension  $N_d$ 
11:     $\{\mathbf{u}(t_n)\}_{n=1,T}^N = \text{LESnets}(\mathcal{G}_\theta, \{\mathbf{u}(t_n)\}_{n=0}^N, \{t_{n=0}\})$ 
12:     $\{\mathbf{u}(t_n)\}_{n=0,T}^N = \{\mathbf{u}(t_n)\}_{n=0}^N + \{\mathbf{u}(t_n)\}_{n=1,T}^N \leftarrow$  Add at dimension  $T$ 
13:     $\{\partial_t \mathbf{u}(t_n)\}_{n=1,T-1} = (\mathbf{u}_{t+1} - \mathbf{u}_{t-1}) / (2\Delta t)$ 
14:     $\{\hat{\mathbf{u}}\}^k = \mathcal{F}(\mathbf{u})$ 
15:     $\mathcal{L}_1 = \nabla \cdot \mathbf{u} = \mathcal{F}^{-1}(ik\hat{\mathbf{u}})$ 
16:     $\{\boldsymbol{\omega}(t_n)\}_{n=0,T}^N = \mathcal{F}^{-1}(ik \times \hat{\mathbf{u}})$ 
17:     $\{\hat{\mathbf{R}}\}^k = \mathcal{F}(\mathbf{u} \times \boldsymbol{\omega}) - ik\hat{\boldsymbol{\tau}}$ 
18:     $\{\hat{\mathbf{p}}\}^k = -\frac{1}{k^2} ik \cdot \hat{\mathbf{R}}$ 
19:     $\mathcal{L}_2 = \partial_t \mathbf{u} + \mathcal{F}^{-1}(\nu k^2 \hat{\mathbf{u}}) - \mathcal{F}^{-1}(\hat{\mathbf{R}}) + \mathcal{F}^{-1}(\hat{\mathbf{p}})$ 
20:     $\mathcal{L}_{PDE} = \sum_{n=1}^{T-1} \|\mathcal{L}_1 + \mathcal{L}_2\|$ 
21:     $\theta \leftarrow \theta - \lambda \cdot \nabla_\theta \mathcal{L}_{PDE}$ 
22:    Append  $\theta$  to  $\Theta$ 
23:  end for
24: Select proper  $\theta^*$  from  $\Theta$  based on relative error during training process.

```

$$Q = \frac{1}{2} (\bar{\Omega}_{ij} \bar{\Omega}_{ij} - \bar{S}_{ij} \bar{S}_{ij}), \quad (18)$$

where $\bar{\Omega}_{ij} = (\partial \bar{u}_i / \partial x_j - \partial \bar{u}_j / \partial x_i) / 2$ is the filtered rotation-rate tensor. In addition, we only learn the mapping once in the training, and give the flow field prediction with longer time steps through iteration during the prediction.

3. Numerical experiments

In this section, we apply the proposed LESnets to predict different incompressible turbulent flows, including 3D decaying homogeneous isotropic turbulence and 3D temporally evolving turbulent mixing layer. We present comparisons between the FNO-based LESnets and IFNO-based LESnets-I models. Loss curves during training are used to evaluate the performance of the model. In *a posteriori* test, a new initial field is generated independently. In this study, we consider the output sample size $T = 10$, and after 25th iterations, we obtain a series of flow fields with a time length of $T = 250$, corresponding $t \approx 5\tau$. By comparing LESnets with traditional large-eddy simulation with the SGS model of SM and the data-driven methods of FNO and IFNO, the accuracy, efficiency and generalization ability of LESnets are verified.

3.1. Decaying homogeneous isotropic turbulence

The direct numerical simulation of forced homogeneous isotropic turbulence (HIT) is performed with the uniform grid resolutions of 128^3 in a cubic box of $(2\pi)^3$ with periodic boundary conditions [50, 60]. The initial velocity field is randomly generated with the Gaussian distribution in spectral space. The initial velocity spectrum of the random velocity field is given by [50]

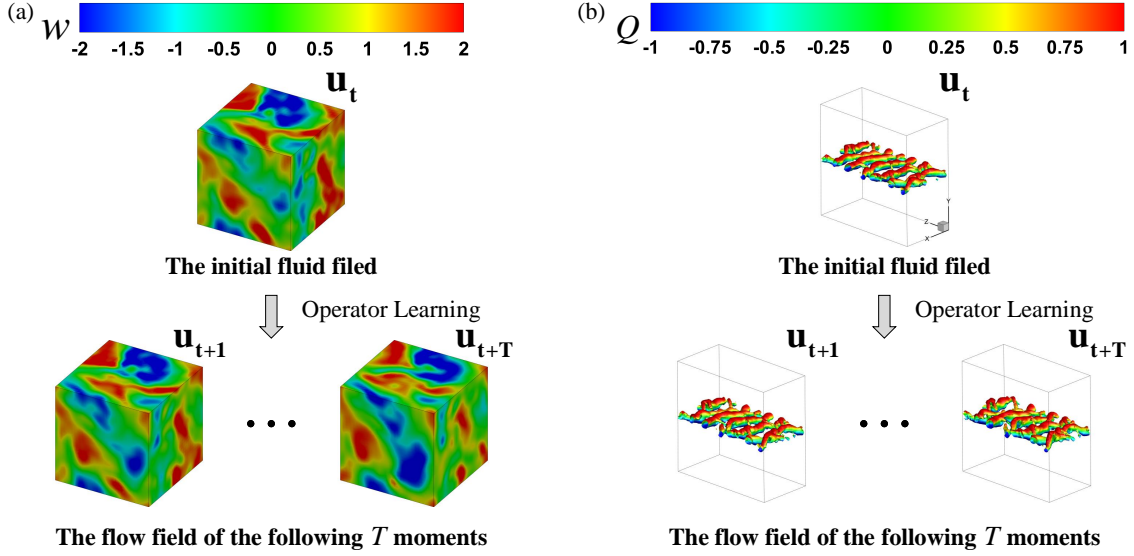


Fig. 4. The inputs and outputs of the neural operators for the two incompressible flow simulation cases of this study. (a) the contours of velocity w in decaying homogeneous isotropic turbulence; (b) the Q criterion in temporally evolving turbulent mixing layer.

$$E(k) = A_0 \left(\frac{k}{k_0} \right)^4 \exp \left[-2 \left(\frac{k}{k_0} \right)^2 \right], \quad (19)$$

where $E(k)$ is the spectrum of kinetic energy per unit mass, k is the wavenumber magnitude in the spectral space. Here, $A_0 = 2.7882$ and $k_0 = 4.5786$. The governing equations Eq.1 and Eq.2 are spatially discretized using the pseudo-spectral method, and a second-order two-step Adams–Bashforth explicit scheme is utilized for time integration [50, 60, 109]. The aliasing error is eliminated by truncating the high wavenumbers of Fourier modes by the two-thirds rule.

The large-scale force is constructed by amplifying the velocity field in the wavenumber space to maintain the total kinetic energy spectrum in the first two wavenumber shells to the prescribed values $E_0(1) = 1.242477$ and $E_0(2) = 0.391356$, respectively [50]. The force $\hat{\mathcal{F}}_i^f(k)$ is expressed as

$$\hat{\mathcal{F}}_i^f(k) = \alpha \hat{\mathcal{F}}_i(k), \quad \text{where } \alpha = \begin{cases} \sqrt{E_0(1)/E(1)}, & 0.5 \leq k \leq 1.5, \\ \sqrt{E_0(2)/E(2)}, & 1.5 \leq k \leq 2.5, \\ 1 & \text{otherwise.} \end{cases} \quad (20)$$

The kinematic viscosity is adopted as $\nu = 0.015625$, leading to the Taylor Reynolds number $Re_\lambda \approx 60$. The DNS time step Δt is set to 0.001. To ensure that the flow has reached a statistically steady state, we keep the force term for a long period (about 10,000 DNS time steps). Then, we remove the external forces and let the turbulence decay freely for 5000 DNS time steps and get the decaying homogeneous isotropic turbulence. We perform 5000 different cases with different initial fields as training data and another 20 cases as test data and the snapshots of the numerical solution are taken every 20 steps as time nodes.

In this work, we consider LES equations Eq. 3 and Eq. 4 with the Smagorinsky model as the physics constraints of the flow. We use the sharp spectral filter: $\hat{G}(k) = H(k_c - |k|)$, $k_c = 10$ is the cutoff wavenumber. The SGS stress in Eq. 4 is modelled by the SM model followed Eq. 5, with Smagorinsky coefficient $C_{smag} = 0.1$.

The fDNS data with tensor size of $[5000 \times 1 \times 32 \times 32 \times 32 \times 3]$ are used for LESnets training, and initial fields of all the 5000 cases are given by snapshot of $10000\Delta t$ filtered of DNS. The fDNS data with tensor size of $[5000 \times 11 \times 32 \times 32 \times 32 \times 3]$ for FNO and IFNO training and $[20 \times 11 \times 32 \times 32 \times 32 \times 3]$ for testing, and the

cases at snapshots from $10000\Delta t \sim 10200\Delta t$. Some important DNS and fDNS parameters are given in Table 1. Here, $\tau \approx 1000\Delta t = 1.00$ is the large-eddy turnover time.

Table 1
Parameters and statistics for DNS and fDNS of decaying HIT.

| Reso.(DNS) | Reso.(fDNS) | Domain | Re_λ | ν | Δt | k_c | τ |
|------------|-------------|------------|--------------|----------|------------|-------|--------|
| 128^3 | 32^3 | $(2\pi)^3$ | 60 | 0.015625 | 0.001 | 10 | 1.00 |

All four neural operator models in this study utilize the same number of the Fourier modes k_{max} , specifically a value of 12. For LESnets and FNO, we use $L = 6$ for the number of Fourier layers, and channel space ‘width’ d_v equals 80 to take full advantage of memory and learning. For LESnets-I and IFNO, we use $L = 20$ for the number of Fourier layers and ‘width’ d_v equals 150 to take full advantage of memory and learning. In order to ensure a fair comparison, we take the same optimization strategy: the initial learning rate for Adam decays from 10^{-3} (4,000 training epochs) to 10^{-4} (6,000 training epochs), 10^{-5} (1,0000 training epochs), 10^{-6} (1,0000 training epochs), a total of 30,000 epochs. The GELU function is chosen as the activation function. LESnets minimizes the PDE loss followed by Eq. 17. For FNO and IFNO method, the training and testing losses are both defined as

$$Loss = \frac{\|u^* - u\|_2}{\|u\|_2}, \quad \text{where } \|A\|_2 = \frac{1}{n} \sqrt{\sum_{k=1}^n |A_k|^2}. \quad (21)$$

Here, u^* denotes the prediction of velocity fields and u is the ground truth. A comparison of the training and testing loss cruve are given in Fig. 5. It is worth noting that due to the different calculation methods of PDE loss and data loss, the magnitude of PDE loss will reach 10^2 in the early iteration, while the data loss given by Eq. 21 is always less than 1.0. As can be seen, the LESnets model has a close test loss compared to the FNO and IFNO model. We also observe that the implicit-based models converge faster compared to other models.

Table 2 shows the minimum Data loss, PDE loss and test loss in the training process. Although FNO achieved the best results, it will be shown in the subsequent verification that FNO can not be generalized to the subsequent flow field in the decaying turbulence, and its stability is poor in long-term prediction.

Table 2
Comparison of minimum training and testing loss of different models in decaying homogeneous isotropic turbulence.

| Model | Data Loss | PDE Loss | Testing Loss |
|-----------|-----------------|----------|-----------------|
| FNO | 0.019680 | N/A | 0.029363 |
| IFNO | 0.021713 | N/A | 0.031973 |
| LESnets | N/A | 0.062677 | 0.057906 |
| LESnets-I | N/A | 0.030308 | 0.059160 |

In the *posteriori* study, five initial turbulence fields are taken from new fDNS fields ($10000\Delta t$) different from the training set, and decay freely for 5000 DNS time steps, and the snapshots of the numerical solution are taken every 20 steps as time nodes. Namely, we want to train models in the $10000\Delta t \sim 10200\Delta t$ interval and make inference in the $10000\Delta t \sim 15000\Delta t$ time interval. The obtained physical quantities are ensemble averaged under five cases. Meanwhile, we will plot the temporal evolutions of flow fields every 0.2τ .

We show the predicted root mean square (rms) values of velocity and vorticity at different time instants in Fig. 6. They represent the statistical characteristics of fluid velocity fluctuation and vortex motion respectively. In the same flow regime as that for the training ($t < 0.2\tau$), all models show excellent results. But as the iterations progress, FNO tends to diverge on the 10th iteration (i.e. $t \approx 2\tau$), eventually deviating from the true value (fDNS). It can be seen that IFNO models are better than traditional FNO models, but implicit methods have almost no improvement on LESnets,

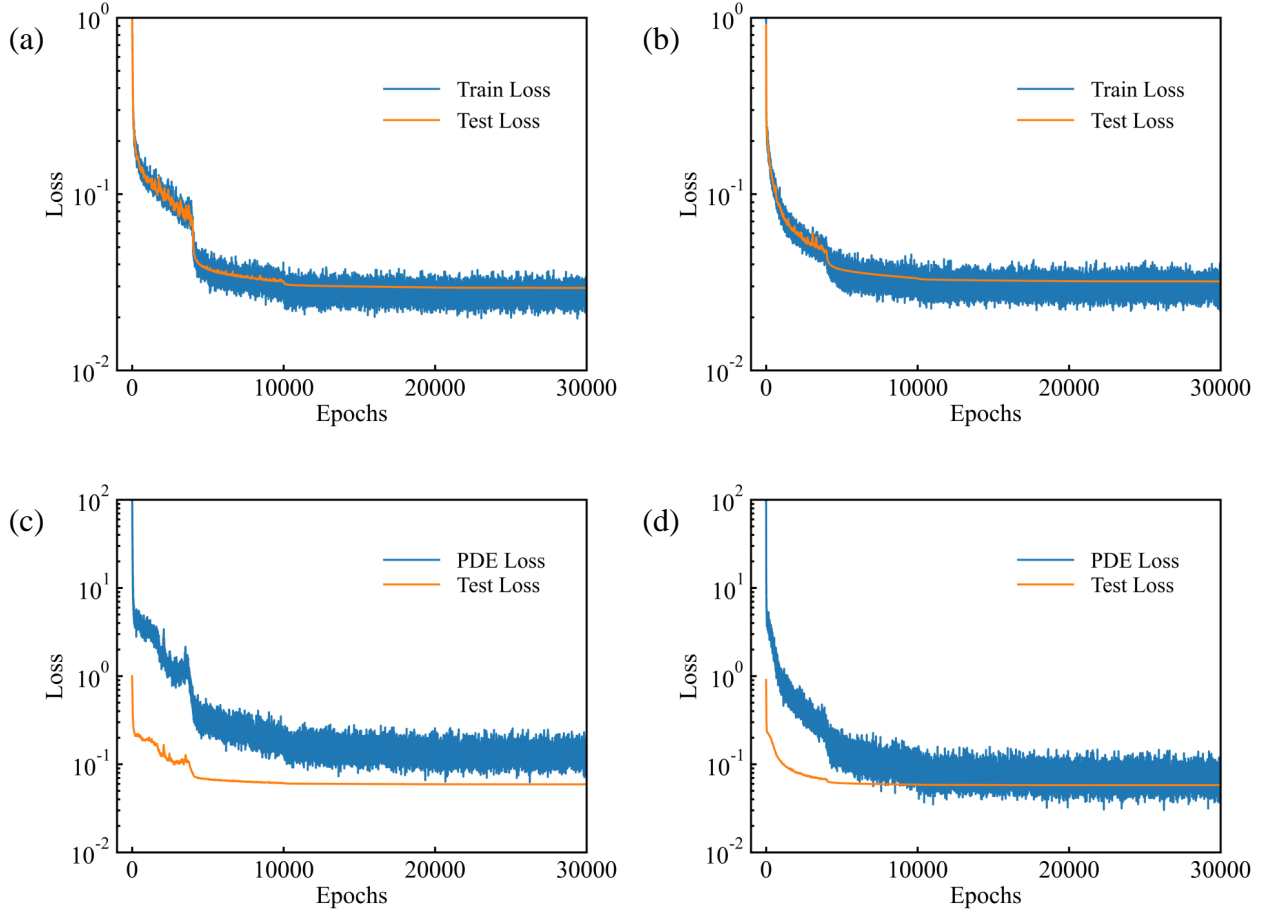


Fig. 5. The evolutions of the loss curves in the decaying HIT: (a) FNO; (b) IFNO; (c) LESnets; (d) LESnets-I

which may be because the optimization potential of models using equation constraints has been fully developed. The traditional SM performs well in the prediction of \bar{u}^{rms} . The results predicted by both LESnets models are stable and close to the values of fDNS. Moreover, the value predicted by FNO-based model is generally large, while the value predicted by LESnets is generally small, which may be caused by the difference of optimization strategies driven by different constraints.

In Fig. 7, we present the temporal evolutions of the turbulent kinetic energy $E_K(t) = \int_0^\infty E(k)dk = \frac{1}{2}(u^{rms})^2$ and the resolved dissipation rate $\bar{\epsilon}$ of SM, FNO, IFNO, LESnets models with fDNS data. It can be seen that the kinetic energy gradually decays from the initial state over time, and FNO model fails to predicting the turbulent kinetic energy at $t \approx \tau$. This observation suggests that the FNO model actually diverges earlier. Here, LESnets models show similar accuracy to SM. The value predicted by IFNO model is generally large, while the value predicted by LESnets is generally small, especially in late stage.

Fig. 8 shows the spectrum of kinetic energy $E(k)$ averaged five cases at different snapshots. It can be seen that with the evolution of time, the turbulent kinetic energy of turbulence decreases at each wavenumber. The energy spectrum predicted by the traditional LES with SM model is slightly lower than fDNS. The FNO model totally mismatch the fDNS at $t \approx 4\tau$. IFNO model exhibits higher values than the fDNS results at all wavenumbers, and conversely, the LESnets-I are slightly lower than the fDNS results. The energy spectra predicted by LESnets are the closest to the SM results, better than IFNO model.

To further examine the LESnets model in predicting multi-scale properties of turbulence, we compute the longitudinal structure functions of the filtered velocity, which are defined by

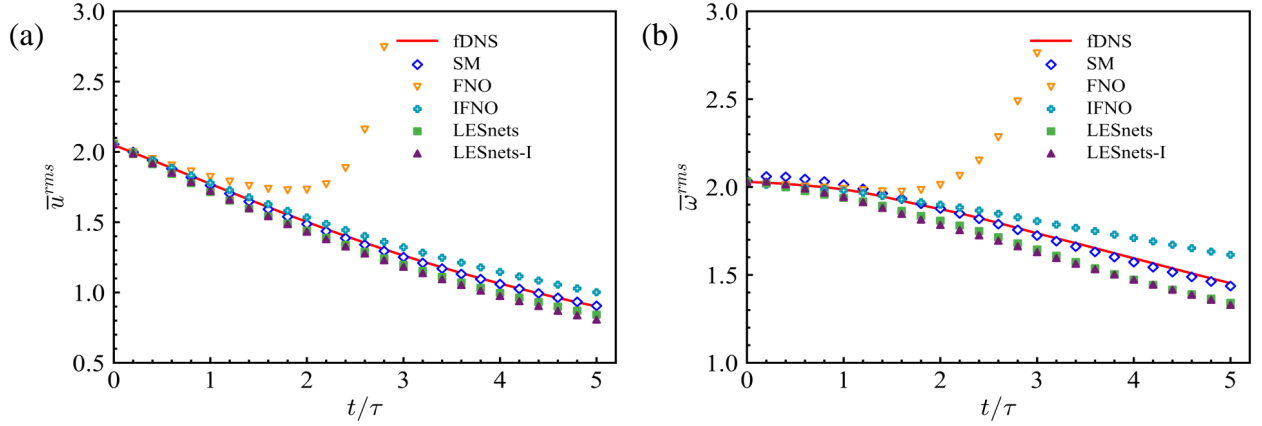


Fig. 6. Temporal evolutions of (a) the velocity rms value and (b) the vorticity rms value for different models in the decaying HIT.

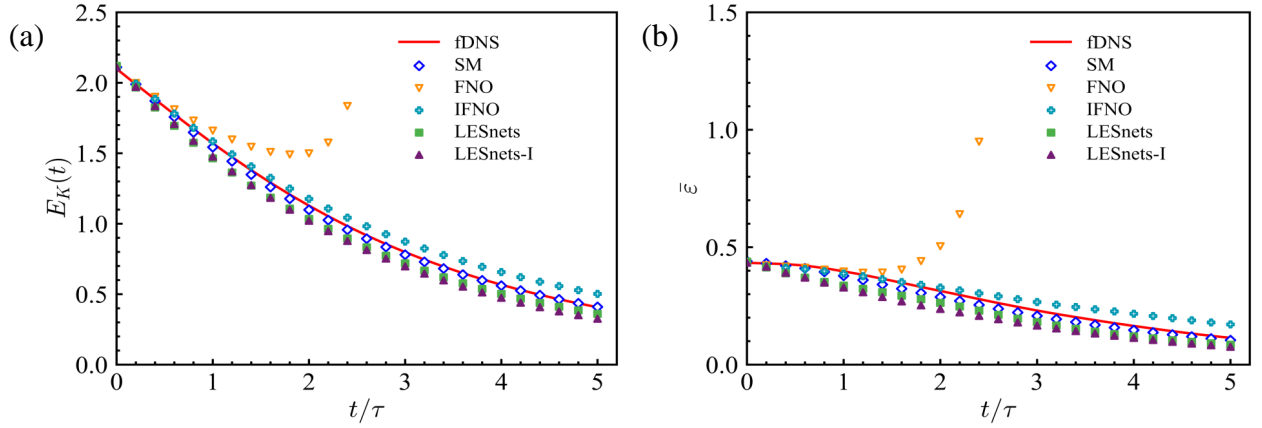


Fig. 7. Temporal evolutions of (a) the turbulent kinetic energy $E_K(t)$ and (b) the average dissipation rate $\bar{\epsilon}$ for different models in decaying HIT.

$$\bar{S}_n(r) = \left\langle \left| \frac{\delta_r \bar{u}}{\bar{u}^{\text{rms}}} \right|^n \right\rangle, \quad (22)$$

where n denotes the order of structure function and $\delta_r \bar{u} = [\bar{\mathbf{u}}(\mathbf{x} + \mathbf{r}) - \bar{\mathbf{u}}(\mathbf{x})] \cdot \hat{\mathbf{r}}$ represents the longitudinal increment of the velocity at the separation \mathbf{r} . Here, $\hat{\mathbf{r}} = \mathbf{r}/|\mathbf{r}|$ is the unit vector.

Fig. 9 compares the second-order and fourth-order structure functions of the filtered velocity for different models at $t \approx \tau$, $t \approx 3\tau$ and $t \approx 5\tau$. It can be seen that the SM model maintains consistent results with fDNS, and the LESnets and LESnets-I predict results that most closely resemble those of SM. Moreover, FNO still gets a divergent result and the IFNO overestimates the structure functions at all distances compared to those of the fDNS data at last time node (i.e. $t \approx 5\tau$). Even at last time node (i.e. $t \approx 5\tau$), LESnets and LESnets-I give a similar results to SM at distances from $r/\bar{\Delta} = 1$ to $r/\bar{\Delta} = 4$.

Furthermore, we compare PDFs of the normalized velocity increments $\delta_r \bar{u}/\bar{u}^{\text{rms}}$ at distance $r = \delta$ at different time instants in Fig. 10. It can be seen that the PDFs of the normalized velocity increments predicted by FNO become wider than the fDNS data as the time increases ($t \approx 4\tau$). The PDF predicted by the IFNO model is also slightly higher than the fDNS results. The SM gives an accurate result but is slightly wider at first time node ($t \approx \tau$). The LESnets and LESnets-I model give the most accurate prediction on the velocity increments, demonstrating the excellent performance of PINO.

The comparison of the above various statistical properties shows that the neural operators with physical constraints

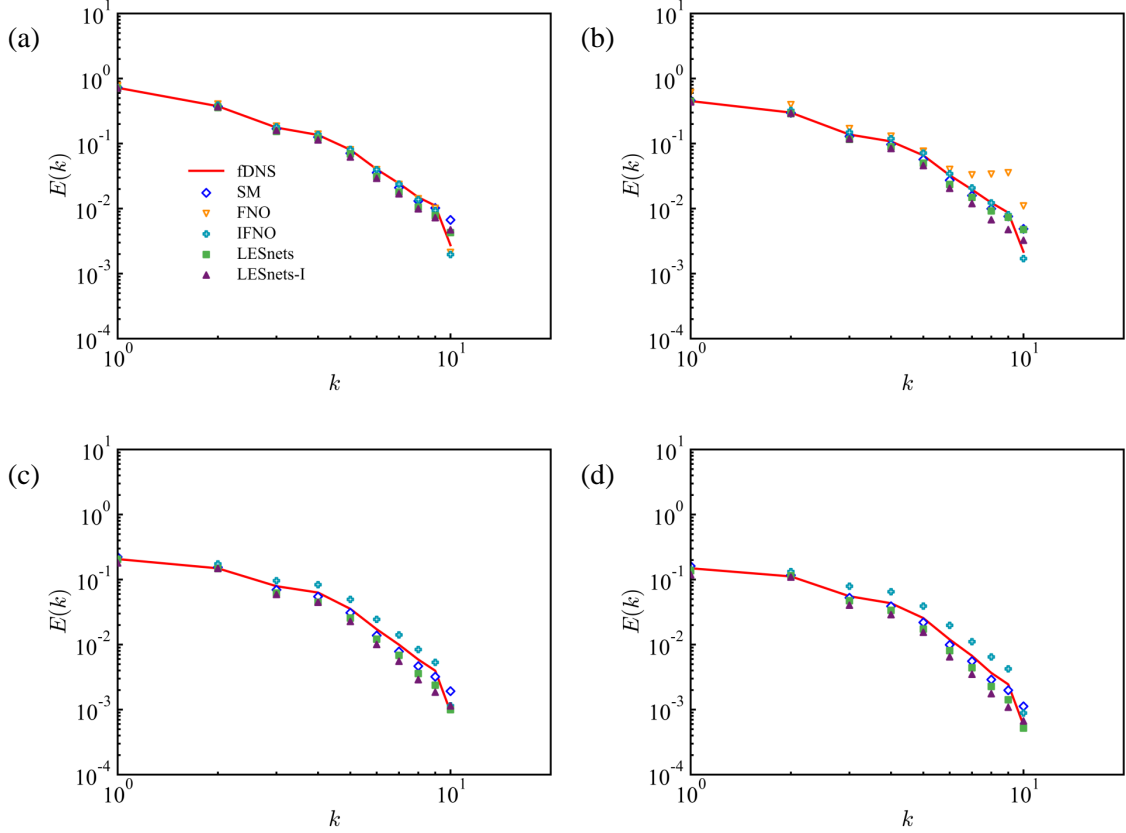


Fig. 8. Spectrum of turbulent kinetic energy of fDNS, SM, FNO, IFNO, LESnets and LESnets-I at (a) $t \approx \tau$; (b) $t \approx 2\tau$; (c) $t \approx 4\tau$ and (d) $t \approx 5\tau$.

perform better than their purely data driven counterparts.

Fig. 11 illustrates the contours of the rms vorticity magnitude fields $|\omega|/\bar{\omega}_{fDNS}^{rms}$ predicted by different models. The instantaneous snapshots are selected on the center of the x-z plane at five different time instants. The first row presents the true values of $|\omega|/\bar{\omega}_{fDNS}^{rms}$ and the other five rows correspond to the prediction results of SM, FNO, IFNO, LESnets and LESnets-I. It can be seen that the traditional SM model is difficult to fully match the results of fDNS in the later stage. Even from the initial field $t = 0$ to $t \approx \tau$, there are drastic changes for the vorticity magnitude. Only the overall spatial distribution of vorticity scales is considered, due to the chaotic nature of turbulence. It is shown that the FNO model completely deviates from the true value, while IFNO overestimates the evolution of vorticity, which may lead to more divergent results in the future. LESnets models can achieve a similar result as traditional large-eddy simulation and data-driven models in the initial stage, and only slightly lower than fDNS in the later stage. Since the large-eddy simulation equations modeled by SM is used as the physics constraints, it is observed that the results of LESnets models are closer to SM, which is also in line with physical intuition.

In addition, we also considered the prediction ability of the model for a specific normalized vorticity value $\bar{\omega}/\bar{\omega}_{fDNS}^{rms} = 1.2$, as shown in Fig. 12. It can be seen that LESnets exhibit a similar accuracy compared with traditional large-eddy simulation methods and data-driven models for a specific iso-surface.

3.2. Temporally evolving turbulent mixing layer

We study the performance of neural operators on large-eddy simulation of a 3-D temporally evolving turbulent mixing layer (TML). The turbulent mixing layer provides a suitable example for studying the effects of nonuniform turbulent shear and mixing on the accuracy of operator learning. The free-shear turbulent mixing layer is governed by Navier–Stokes equations Eq. 1 and Eq. 2 without the forcing term. The mixing layer is numerically simulated in a

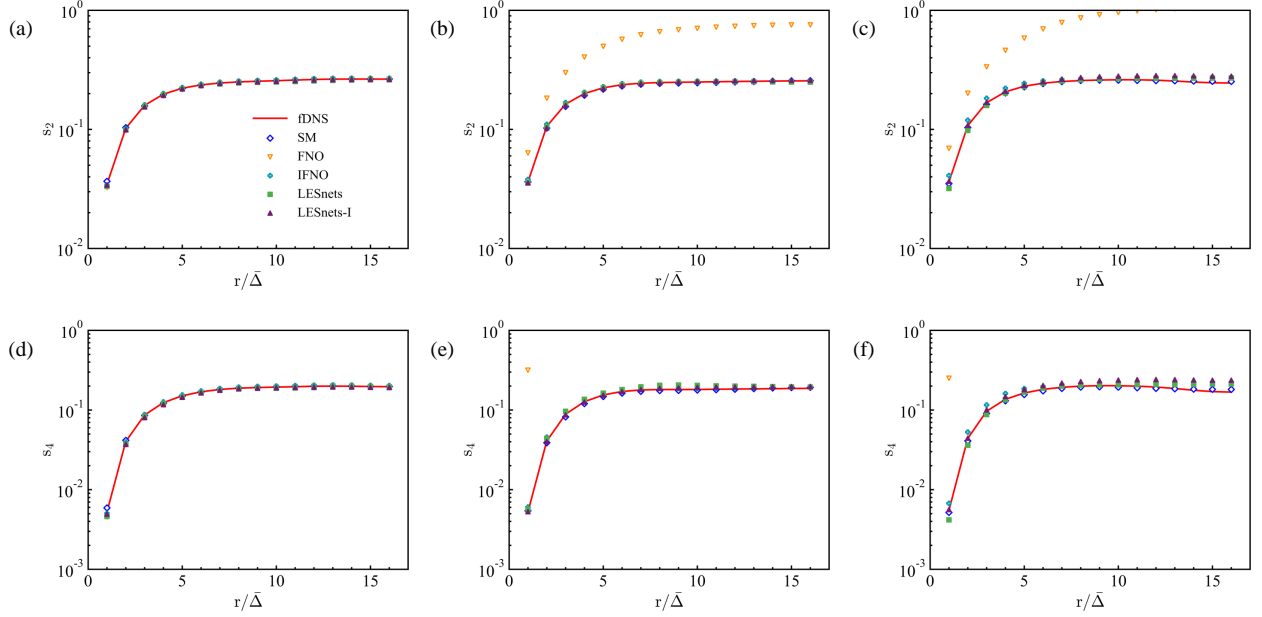


Fig. 9. Second-order and fourth-order structure functions of the LES using different models in the decaying HIT at different time instants (a) first-order, $t \approx \tau$; (b) first-order, $t \approx 3\tau$ and (c) first-order, $t \approx 5\tau$ (d) second-order, $t \approx \tau$; (e) second-order, $t \approx 3\tau$ and (f) second-order, $t \approx 5\tau$.

cuboid domain with lengths $L_1 \times L_2 \times L_3 = 8\pi \times 8\pi \times 4\pi$ using a uniform grid resolution of $N_1 \times N_2 \times N_3 = 256 \times 256 \times 128$. Here, $x_1 \in [-L_1/2, L_1/2]$, $x_2 \in [-L_2/2, L_2/2]$, $x_3 \in [-L_3/2, L_3/2]$ denote the streamwise, normal, and spanwise directions, respectively.

The initial streamwise velocity is given by [56, 57].

$$u_1 = \frac{\Delta U}{2} \left[\tanh\left(\frac{x_2}{2\delta_\theta^0}\right) - \tanh\left(\frac{x_2 + L_2/2}{2\delta_\theta^0}\right) - \tanh\left(\frac{x_2 - L_2/2}{2\delta_\theta^0}\right) \right] + \lambda_1. \quad (23)$$

Here, $-L_2/2 \leq x_2 \leq L_2/2$, $\delta_\theta^0 = 0.08$ is the initial momentum thickness and $\Delta U = U_2 - U_1 = 2$ is the velocity difference between two equal and opposite free streams across the shear layer [57]. The kinematic viscosity is adopted as $\nu = 0.008$. The momentum thickness quantifies the range of turbulence region in the mixing layer, which is given by [55]

$$\delta_\theta = \int_{-L_2/4}^{L_2/4} \left[\frac{1}{4} - \left(\frac{\langle \bar{u}_1 \rangle}{\Delta U} \right)^2 \right] dx_2. \quad (24)$$

Table 3

Parameters and statistics for DNS and fDNS at a grid resolution of TML

| Reso.(DNS: $N_X \times N_Y \times N_Z$) | Reso.(fDNS: $N_X \times N_Y \times N_Z$) | Domain | Re_θ^0 | ν | Δt | δ_θ^0 | ΔU |
|--|---|--------------------------------|---------------|-------|------------|-------------------|------------|
| $256 \times 256 \times 128$ | $64 \times 64 \times 32$ | $8\pi \times 8\pi \times 4\pi$ | 320 | 0.008 | 0.001 | 0.08 | 2 |

The initial normal and spanwise velocity perturbations are given as $u_2 = \lambda_2, u_3 = \lambda_3$, respectively. Here, $\lambda_1, \lambda_2, \lambda_3 \sim \mathcal{N}(\mu, \sigma_2)$, i.e., $\lambda_1, \lambda_2, \lambda_3$ satisfy the Gaussian random distribution. The expectation of the distribution is $\mu = 0$, and the variance of the distribution is $\sigma_2 = 0.01$. The Reynolds number based on the momentum thickness Re_θ is defined as $Re_\theta = \Delta U \delta_\theta / \nu_\infty$. Here, the kinematic viscosity of shear layer is set to $\nu_\infty = 5 \times 10^{-4}$, so the initial

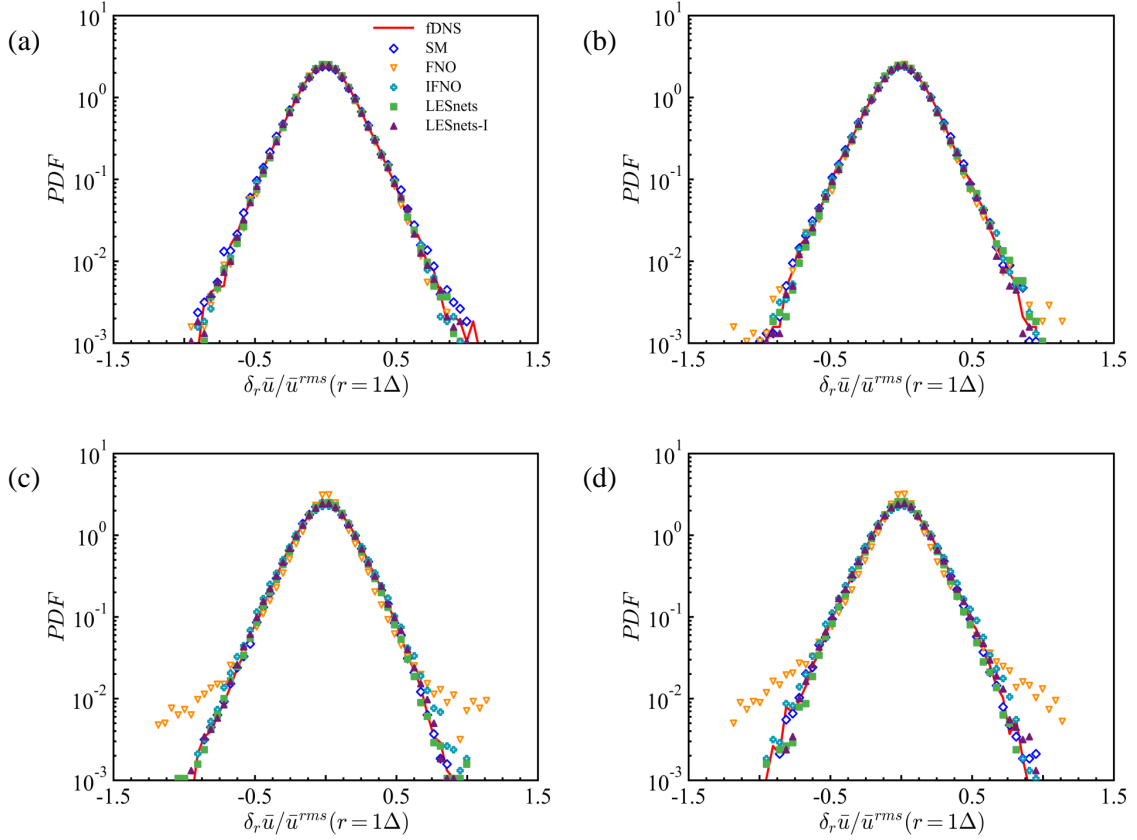


Fig. 10. Spectrum of turbulent kinetic energy of fDNS, SM, FNO, IFNO, LESnets and LESnets-I at (a) $t \approx \tau$; (b) $t \approx 2\tau$; (c) $t \approx 4\tau$ and (d) $t \approx 5\tau$.

momentum thickness Reynolds number is $Re_\theta^0 = 320$. To mitigate the impact of the top and bottom boundaries on the central mixing layer, two numerical diffusion buffer zones are implemented to the vertical edges of the computational domain [36]. The periodic boundary conditions in all three directions are utilized, and the pseudo-spectral method with the two-thirds dealiasing rule is employed. An explicit two-step Adam–Bashforth scheme is chosen as the time advancing scheme.

Similarly, we use the same sharp spectral filter: $\hat{G}(k) = H(k_c - |k|)$ to filter the DNS data as for decaying HIT. Here, the filtering scale is $\bar{\Delta} = 8h_{DNS}$, where h_{DNS} is the grid spacing of DNS. The filter-to-grid ratio $FGR = \bar{\Delta}/h_{LES} = 2$ is utilized, and then, the corresponding grid resolution of fDNS: $64 \times 64 \times 32$ can be obtained. The SGS model SM is used with Smagorinsky coefficient $C_{smag} = \sqrt{0.001}$.

We perform numerical simulations for 200 sets of distinct initial fields for training and 5 sets for testing, and save the results for 100 temporal snapshots for each initial field. The time interval for each snapshot is $20\Delta t$. The data sizes are $[200 \times 100 \times 64 \times 64 \times 32 \times 3]$ and $[5 \times 100 \times 64 \times 64 \times 32 \times 3]$, respectively. For LESnets, one snapshot is taken every 10 steps as the initial input; meanwhile, for FNO and IFNO, all of the above data are required as input. Therefore, the fDNS data with tensor size of $[2000 \times 1 \times 64 \times 64 \times 32 \times 3]$ are used for LESnets training, the fDNS data with tensor size of $[2000 \times 11 \times 64 \times 64 \times 32 \times 3]$ are used for FNO and IFNO training and the fDNS data with tensor size of $[50 \times 11 \times 32 \times 32 \times 32 \times 3]$ are used for testing. In training process, we use data from $T = 0 \sim 100$ time periods for training, but in the prediction task, we make the model to advance to $T = 250$.

In this study, we maintain the same parameter settings, activation function and optimizer as in decaying HIT problem. Here we reduced the number of training epochs, using the same optimizer Adam decays from 10^{-3} (4,000 training epochs) to 10^{-4} (6,000 training epochs), 10^{-5} (1,000 training epochs), a total of 20,000 epochs. The loss of Eq. 17 is used for LESnets, and the loss of Eq. 21 is used for FNO and IFNO.

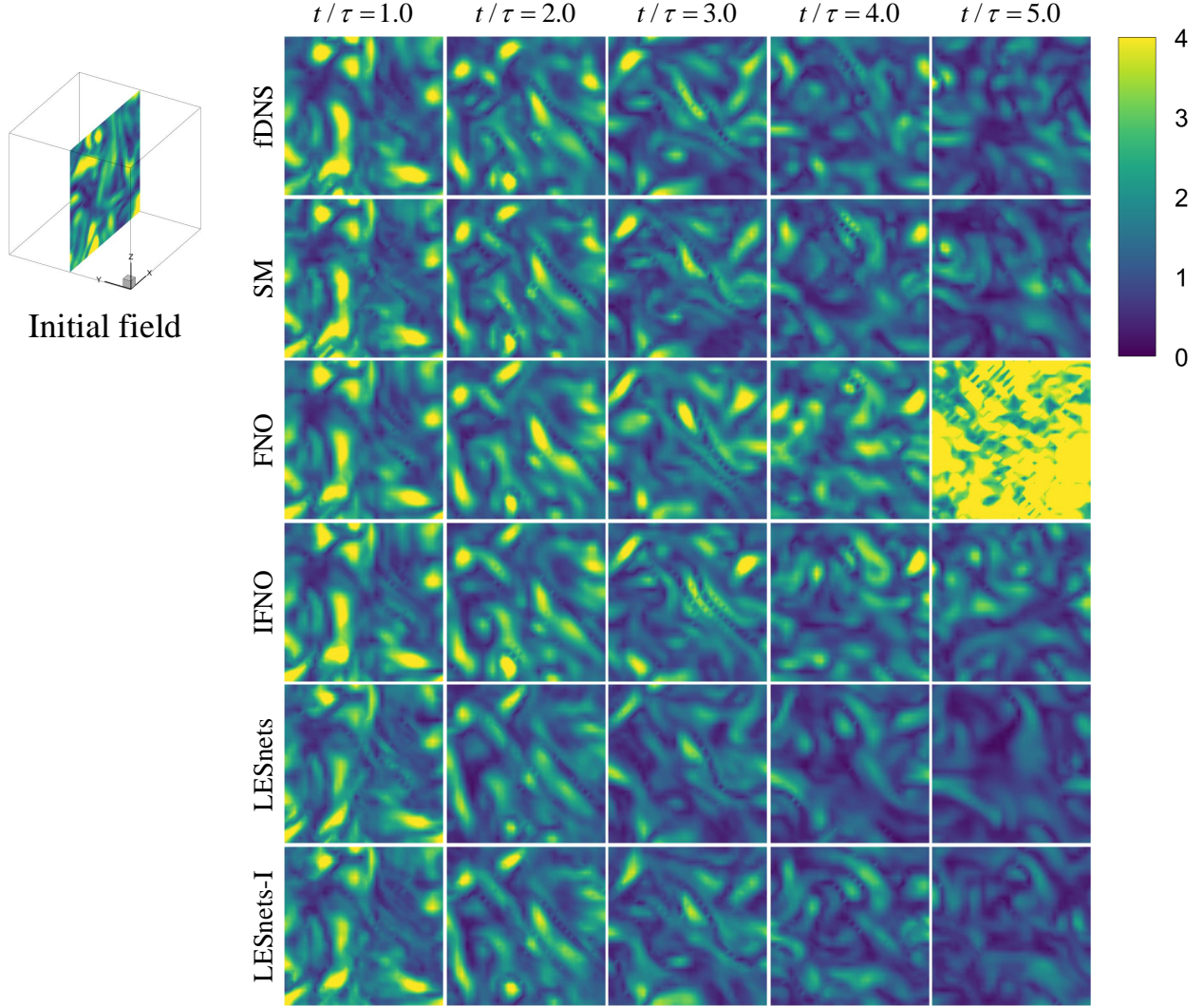


Fig. 11. The rms vorticity magnitude fields $|\omega|/\bar{\omega}_{fDNS}^{rms}$ (at the center of x - z plane) of the true simulation and model predictions of Large-eddy simulation equation from $t \approx \tau$ to $t \approx 5\tau$ time units.

A comparison of the training and testing loss curve are given in Fig. 13. As can be seen, the LESnets model has a similar loss compared to the FNO and IFNO models. The test error of LESnets is larger than data-driven models.

After training, five more groups of data with different initial fields are generated to perform *a posteriori* analysis, each containing twenty five nodes. Here, twenty five nodes are equivalent to two hundreds and fifty time units $t/\tau_\theta = 250$ normalized by $\tau_\theta = \delta_\theta^0/\Delta U = 20\Delta t$. Fig. 14 compares the temporal evolutions of the streamwise turbulent kinetic energy $E_{k1} = \frac{1}{2}(\sqrt{\langle u_1 u_1 \rangle})^2$ and the momentum thickness δ_θ of SM, FNO, IFNO, LESnets and LESnets-I models. It is interesting to note that FNO does not diverge in the TML problem. In addition, the implicit iteration method is no better than the traditional FNO model for the streamwise turbulent kinetic energy. In terms of momentum layer thickness, the data-driven model has a better prediction accuracy than the large-eddy simulation method. The result predicted by LESnets is even better than that by SM method.

Furthermore, we compare PDFs of the spanwise velocity increment $\delta_{r3}\bar{u}/\bar{u}^{rms}$ with distance $r = \Delta$ at different time instants in Fig. 15. It can be seen that the PDFs of the spanwise velocity increment predicted by SM is slightly narrower than fdNS, while the PDFs predicted by IFNO is wider than the fdNS data. The PDF predicted by the FNO model and LESnets-I is closest to the fdNS results.

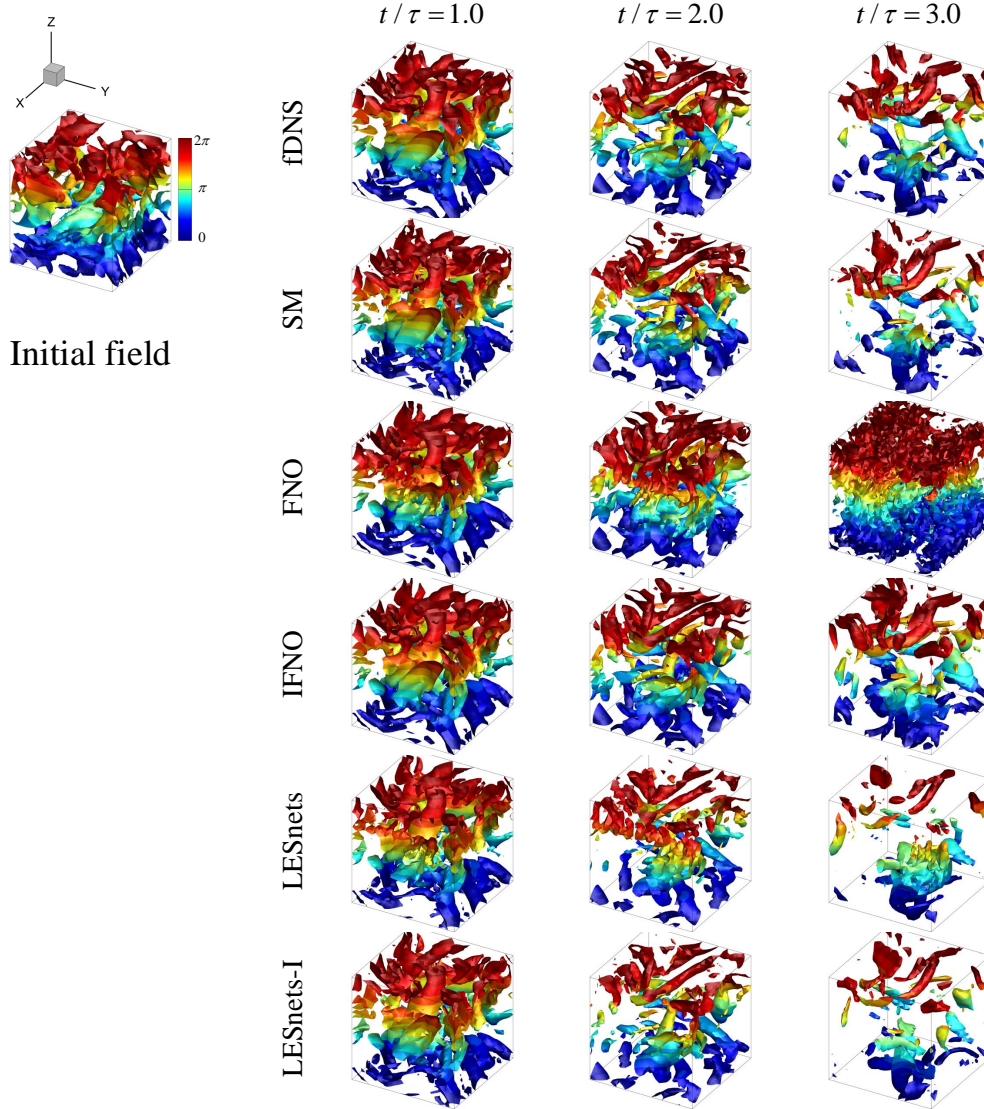


Fig. 12. The specific normalized vorticity $\bar{\omega}/\bar{\omega}_{\text{fDNS}}^{\text{rms}} = 1.2$ fields (at the center of X-Z plane) of the true simulation and model predictions of large-eddy simulation equation from $t \approx \tau$ to $t \approx 3\tau$ time units.

Finally, we compare the vortex structures predicted by the different models with fDNS data. The Q criterion has been widely used for visualizing vortex structures in turbulent flows [53, 54], where Q is defined by Eq. 18. Fig. 16 displays the instantaneous isosurfaces of $Q = 0.2$ at five time nodes colored by the streamwise velocity. In the prediction of vortex structure, LESnets models can maintain a similar accuracy with large-eddy simulation method and data-driven models.

3.3. Computational efficiency

We present the training and inference times for four types of models across two turbulence prediction tasks, and compare them with traditional LES method to evaluate the efficiency of each type of model. Table 4 compares the training cost of one epoch, the inference cost of 250 prediction steps (i.e. 5000 DNS advance steps), number of parameters of the model, GPU memory-usage for different models on predictions of decaying HIT. For decaying HIT, the neural network models are trained and test on an Nvidia A100 40G PCIe GPU, while the CPU used for loading model

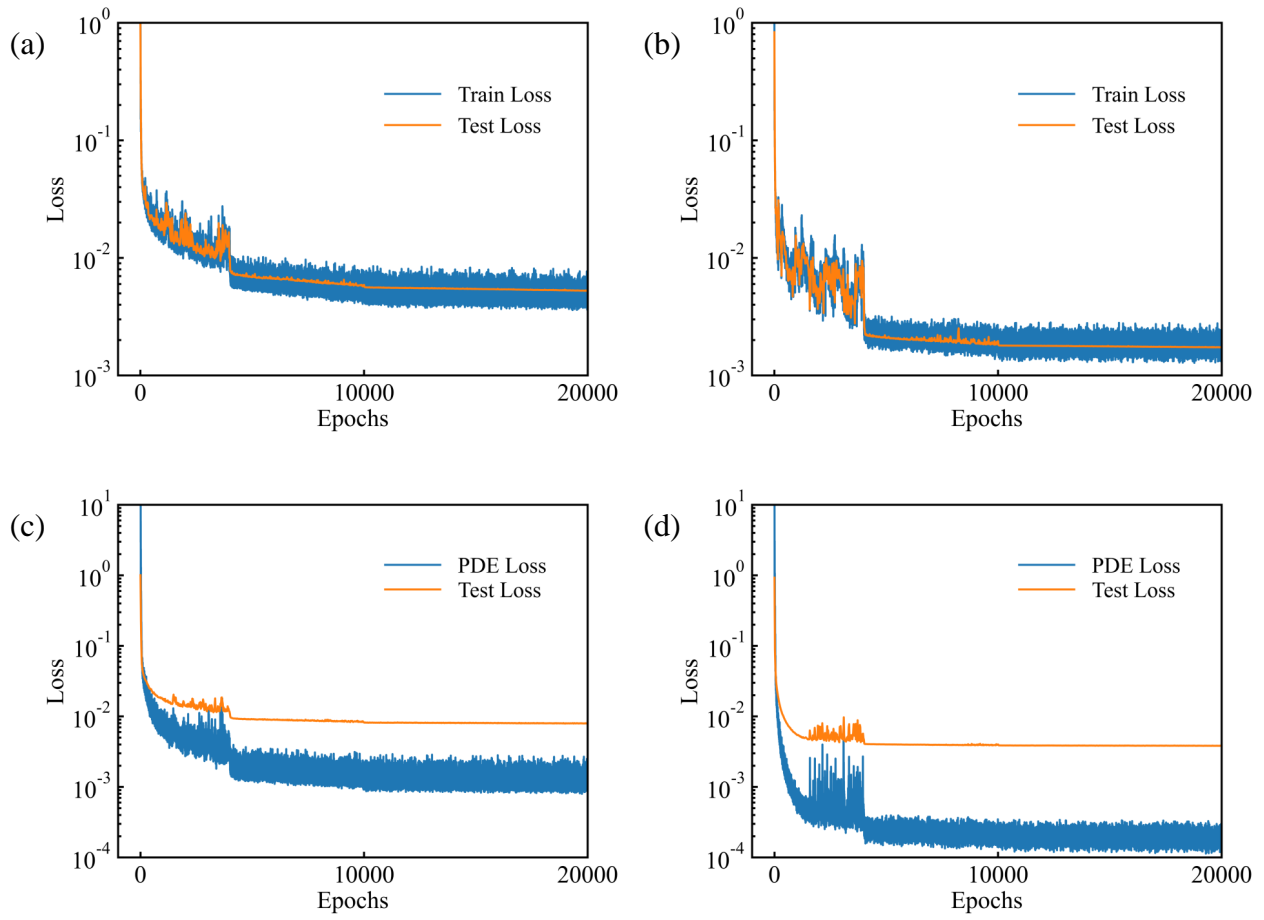


Fig. 13. The evolutions of the loss curves in the TML: (a) FNO; (b) IFNO; (c) LESnets; (d) LESnets-I

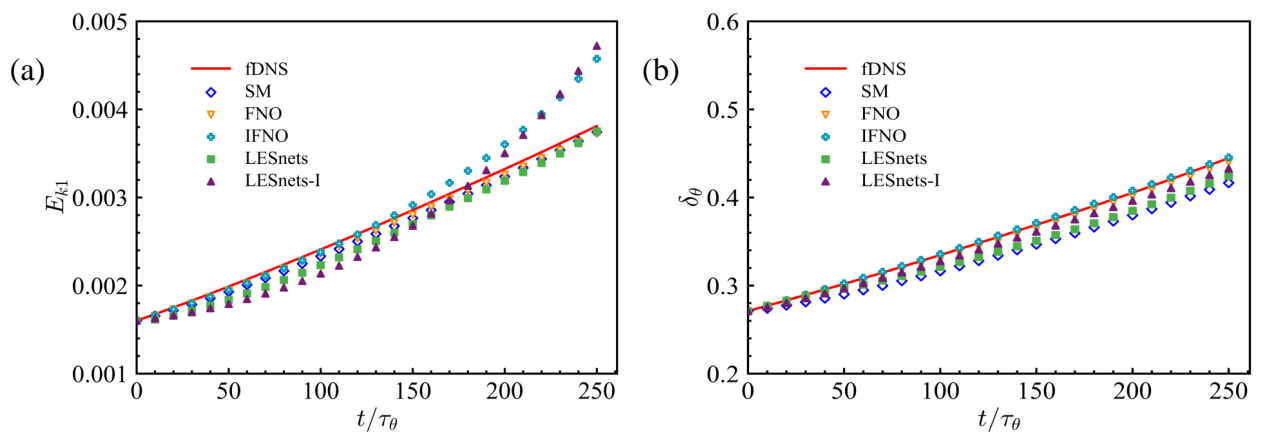


Fig. 14. Temporal evolutions of (a) the streamwise turbulent kinetic energy E_{k1} and (b) the momentum thickness δ_θ for LES using different models in TML.

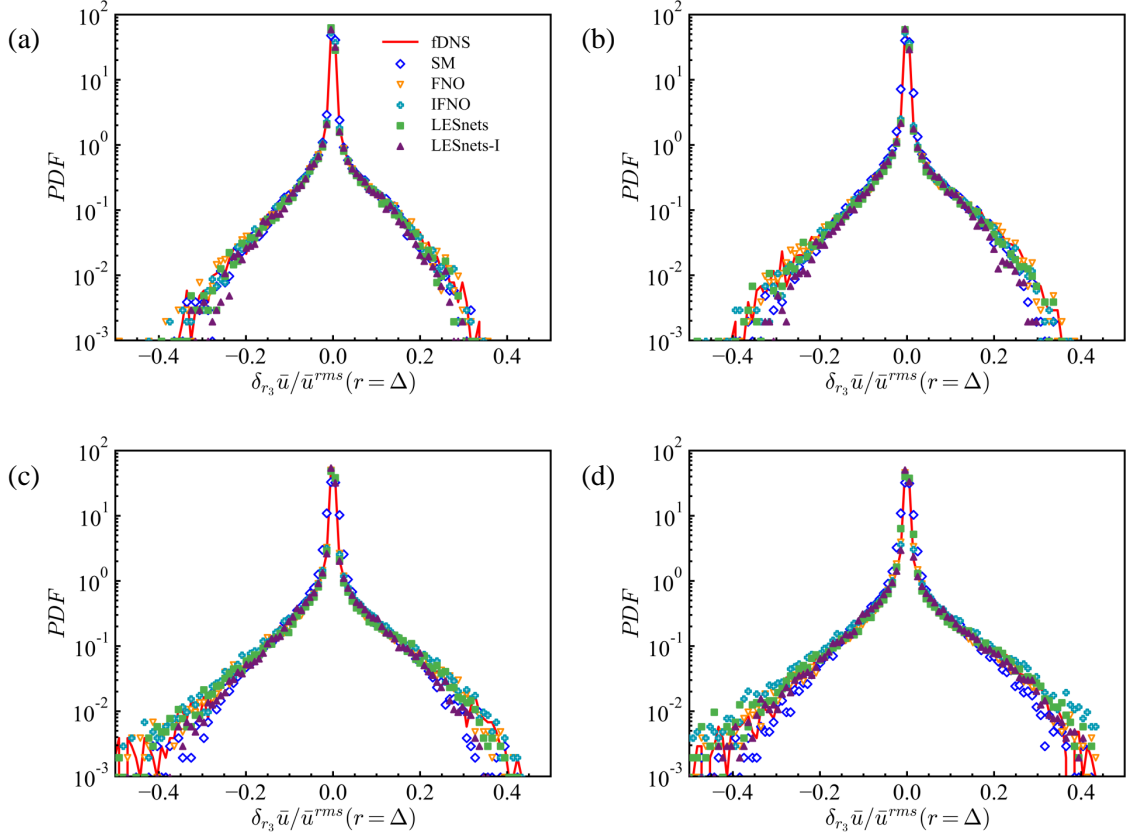


Fig. 15. The PDFs of the spanwise velocity increment of fDNS, SM, FNO, IFNO, LESnets and LESnets-I at (a) $t \approx 50\tau_\theta$; (b) $t \approx 100\tau_\theta$; (c) $t \approx 200\tau_\theta$ and (d) $t \approx 250\tau_\theta$.

parameters and data is an Intel(R) Xeon(R) Gold 6248R CPU @ 3.00 GHz. The LES simulations are implemented on a computing cluster, where the type of CPU is Intel Xeon Gold 6148 with 16 cores each @2.40 GHz. The Table 4 illustrates that LESnets spend only 1% to 5% more time on training than their corresponding data-driven models, while maintaining a similar efficiency as data-driven models in terms of model parameters, computational memory, and inference time. In terms of inference efficiency, LESnets can get up to 30 times faster than LES simulations. Although data-driven models have the same inference efficiency, the time to prepare the data will also be enormous, and LESnets only need to acquire initial fields for training.

Table 4

Computational efficiency of different approaches on decaying HIT.

| Method | Training (s/epoch) | Number of parameters ($\times 10^6$) | GPU memory-usage (GB) | Inference (s) |
|-----------|--------------------|--|-----------------------|---------------|
| DSM | N/A | N/A | N/A | 45.62 |
| FNO | 0.39 | 1061.7 | 38.2 | 1.50 |
| IFNO | 2.17 | 622.1 | 37.7 | 11.84 |
| LESnets | 0.41 | 1061.7 | 38.0 | 1.48 |
| LESnets-I | 2.20 | 622.1 | 37.6 | 11.76 |

Since in temporally evolving turbulent mixing layer, the size of the flow field data is larger, the neural network models are trained and test on an Nvidia A100 80G PCIe GPU, where the CPU type is AMD EPYC 7763 @2.45 GHz. The LES simulations are implemented on the same computing cluster as in the situation of decaying HIT. The Table 5

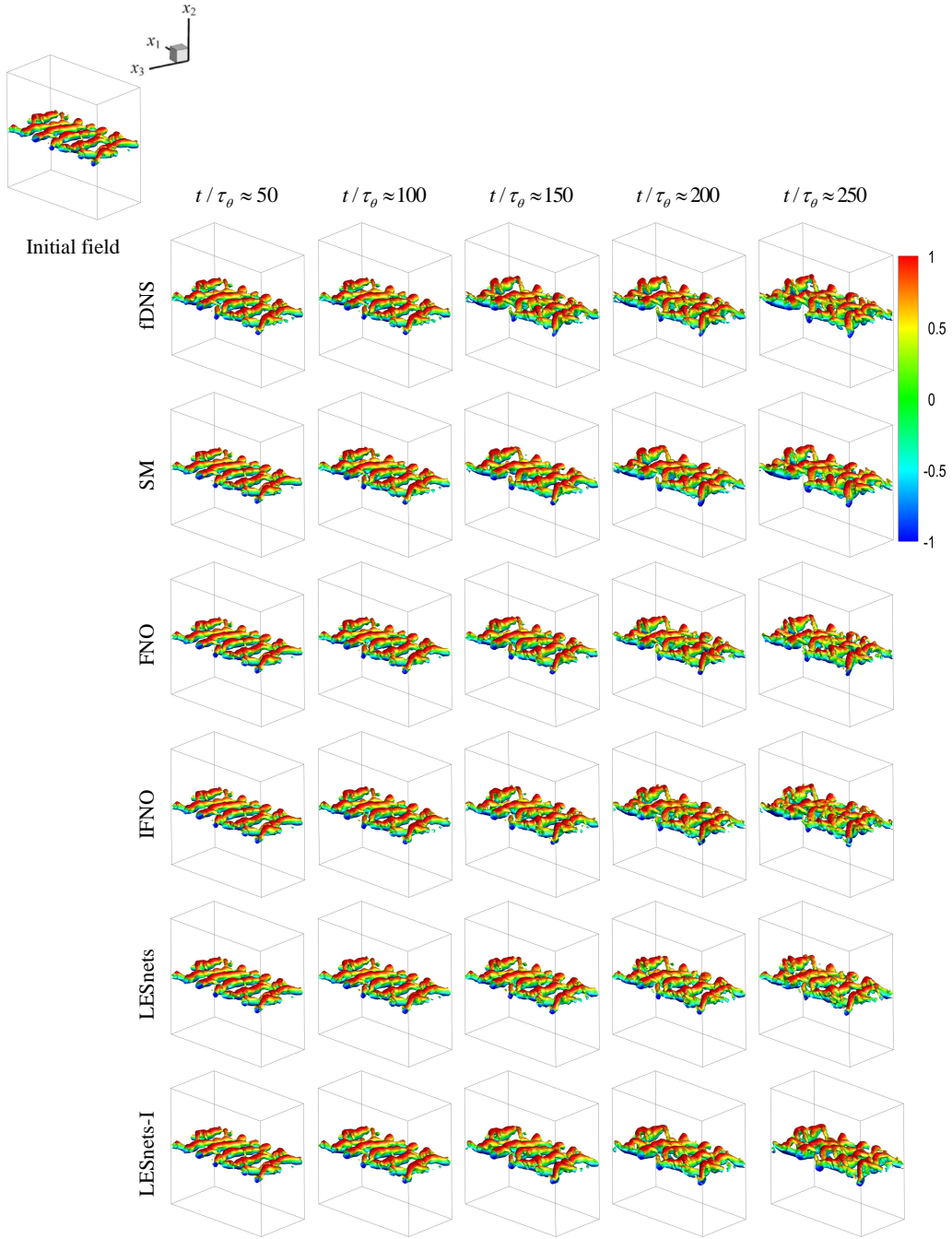


Fig. 16. The iso-surface of the Q criterion at $Q = 0.2$ colored by the streamwise velocity u at $t/\tau_\theta \approx 50, 100, 150, 200, 250$ in the free-shear turbulent mixing layer.

illustrates that LESnets maintain the same efficiency as data-driven models in training time, and the actual prediction time of LESnets was merely 3.18 seconds, which is 1/40 of the time taken by the LES simulation.

Table 5

Computational efficiency of different approaches on temporally evolving turbulent mixing layer.

| Method | Training (s/epoch) | Number of parameters ($\times 10^6$) | GPU memory-usage (GB) | Inference (s) |
|-----------|--------------------|--|-----------------------|---------------|
| DSM | N/A | N/A | N/A | 126.79 |
| FNO | 0.69 | 1061.7 | 53.5 | 3.19 |
| IFNO | 3.95 | 622.1 | 77.4 | 21.83 |
| LESnets | 0.70 | 1061.7 | 53.5 | 3.18 |
| LESnets-I | 3.96 | 622.1 | 77.4 | 18.31 |

4. Conclusion

Simulations of three-dimensional (3D) nonlinear partial differential equations (PDEs) are of great importance in engineering applications. Physics constraints have been widely used to enhance neural networks or operator learning. According to our investigation, no one has used large-eddy simulation equations as PDE constraints to train a physics informed neural operator for three-dimensional turbulence prediction.

In this study, we explore the effectiveness of physics informed neural operator (PINO) to directly predict 3D incompressible turbulent flows, including decaying homogeneous isotropic turbulence and temporally evolving turbulent mixing layer. We develop the LESnets based on the constraint of large-eddy simulation equations and two neural operator models: FNO and IFNO. The input and output of operator learning are three-dimensional velocity fields. The PDE loss is then used as an optimization target to optimize the network parameters, which makes it no longer using the initial field as supervised data to train neural operator. The problems we consider obey the periodic boundary condition, which is satisfied automatically by spectral method. Moreover, since there is no need for the real data of the output as the label data, the length and interval of LESnets output time period are arbitrary. Thus, there is no need to prepare a large amount of data due to the change of the output target. This training method makes LESnets have the same or even better ability to generalize beyond the unseen timeline compared with the data-driven model.

By using only physical constraints to train LESnets, from the results of two turbulence prediction tasks, LESnets with the two neural operators maintain or even outperform the data-driven model and the large-eddy simulation method. In terms of computational efficiency, LESnets only take 1% to 5% more training time than data-driven models, and maintain a similar inference efficiency as data-driven models, achieving a 40x acceleration compared to traditional LES simulations.

The current study for predicting turbulence using LESnets is the first attempt to evaluate the PINO performance on LES of 3D turbulence. While the present results are encouraging, it is crucial to develop the PINO method for more challenging problems. The accuracy of LESnets also rely on the traditional large-eddy simulation methods and the network architecture of data-driven models. Thus, using better SGS models and neural operator models can make LESnets more accurate. In addition, it is necessary to use other discrete methods to calculate the loss function in the situations of non-uniform grids and complicated boundary conditions.

CRedit authorship contribution statement

Sunan Zhao: Conceptualization, Methodology, Investigation, Coding, Validation, Writing - original draft preparation, Writing - reviewing and editing. **Zhijie Li:** Conceptualization, Methodology, Investigation, Coding, Writing - reviewing and editing. **Boyu Fan:** Conceptualization, Methodology, Investigation, Coding. **Yunpeng Wang:** Conceptualization, Investigation, Writing - reviewing and editing. **Huiyu Yang:** Conceptualization, Investigation, Writing - reviewing and editing. **Jianchun Wang:** Conceptualization, Methodology, Investigation, Supervision, Writing - reviewing and editing, Project administration, Funding acquisition.

Declaration of competing interest

The authors declare that they have no known competing financial interests or personal relationships that could have appeared to influence the work reported in this paper.

ACKNOWLEDGMENTS

This work was supported by the National Natural Science Foundation of China (NSFC Grant Nos. 12172161, 12302283, 92052301, and 12161141017), by the Shenzhen Science and Technology Program (Grant No. KQTD20180-411143441009), and by Department of Science and Technology of Guangdong Province (Grant No. 2019B21203001, No. 2020B1212030001, and No. 2023B1212060001). This work was also supported by Center for Computational Science and Engineering of Southern University of Science and Technology, and by National Center for Applied Mathematics Shenzhen (NCAMS).

References

- [1] Z. Zou, X. Meng, G. E. Karniadakis, Uncertainty quantification for noisy inputs–outputs in physics-informed neural networks and neural operators, *Computer Methods in Applied Mechanics and Engineering* 433 (2025) 117479.
- [2] Y. Chen, D. Huang, D. Zhang, J. Zeng, N. Wang, H. Zhang, J. Yan, Theory-guided hard constraint projection (HCP): A knowledge-based data-driven scientific machine learning method, *Journal of Computational Physics* 445 (2021) 110624.
- [3] S. A. Faroughi, N. M. Pawar, C. Fernandes, M. Raissi, S. Das, N. K. Kalantari, S. Kourosh Mahjour, Physics-guided, physics-informed, and physics-encoded neural networks and operators in scientific computing: Fluid and solid mechanics, *Journal of Computing and Information Science in Engineering* 24 (4) (2024) 040802.
- [4] B. Alkin, A. Fürst, S. Schmid, L. Gruber, M. Holzleitner, J. Brandstetter, Universal Physics Transformers: A Framework For Efficiently Scaling Neural Operators, *arXiv e-prints* (Feb. 2024).
- [5] S. G. Rosofsky, E. Huerta, Magnetohydrodynamics with physics informed neural operators, *Machine Learning: Science and Technology* 4 (3) (2023) 035002.
- [6] K. Azizadenesheli, N. Kovachki, Z. Li, M. Liu-Schiaffini, J. Kossaifi, A. Anandkumar, Neural operators for accelerating scientific simulations and design, *Nature Reviews Physics* (2024) 1–9.
- [7] S. Rezaei, A. Moeineddin, M. Kaliske, M. Apel, Integration of physics-informed operator learning and finite element method for parametric learning of partial differential equations, *arXiv preprint arXiv:2401.02363* (2024).
- [8] C. Wang, J. Berner, Z. Li, D. Zhou, J. Wang, J. Bae, A. Anandkumar, Beyond Closure Models: Learning Chaotic-Systems via Physics-Informed Neural Operators, *arXiv preprint arXiv:2408.05177* (2024).
- [9] H. Maust, Z. Li, Y. Wang, D. Leibovici, O. Bruno, T. Hou, A. Anandkumar, Fourier continuation for exact derivative computation in physics-informed neural operators, *arXiv preprint arXiv:2211.15960* (2022).
- [10] C. Lorusso, Z. Li, A. B. Farimani, Physics informed token transformer for solving partial differential equations, *Machine Learning: Science and Technology* 5 (1) (2024) 015032.
- [11] T. Li, L. Biferale, F. Bonaccorso, M. A. Scarpolini, M. Buzicotti, Synthetic Lagrangian turbulence by generative diffusion models, *Nature Machine Intelligence* (2024) 1–11.
- [12] I. Zanardi, S. Venturi, M. Panesi, Adaptive physics-informed neural operator for coarse-grained non-equilibrium flows, *Scientific reports* 13 (1) (2023) 15497.
- [13] Z. Mao, A. D. Jagtap, G. E. Karniadakis, Physics-informed neural networks for high-speed flows, *Computer Methods in Applied Mechanics and Engineering* 360 (2020) 112789.
- [14] D. Zhang, Y. Chen, S. Chen, Filtered Partial Differential Equations: a robust surrogate constraint in physics-informed deep learning framework, *arXiv preprint arXiv:2311.03776* (2023).
- [15] L. Lu, P. Jin, G. Pang, Z. Zhang, G. E. Karniadakis, Learning nonlinear operators via DeepONet based on the universal approximation theorem of operators, *Nature machine intelligence* 3 (3) (2021) 218–229.
- [16] S. Wang, X. Yu, P. Perdikaris, When and why PINNs fail to train: A neural tangent kernel perspective, *Journal of Computational Physics* 449 (2022) 110768.
- [17] P. C. Di Leoni, L. Lu, C. Meneveau, G. E. Karniadakis, T. A. Zaki, Neural operator prediction of linear instability waves in high-speed boundary layers, *Journal of Computational Physics* 474 (2023) 111793.
- [18] O. Ovidia, V. Oommen, A. Kahana, A. Peyvan, E. Turkel, G. E. Karniadakis, Real-time inference and extrapolation via a diffusion-inspired temporal transformer operator (DiTTO), *arXiv preprint arXiv:2307.09072 v2* (2023).
- [19] B. Raonic, R. Molinaro, T. De Ryck, T. Rohner, F. Bartolucci, R. Alaifari, S. Mishra, E. de Bézenac, Convolutional neural operators for robust and accurate learning of PDEs, *Advances in Neural Information Processing Systems* 36 (2024).
- [20] Y. Lyu, X. Zhao, Z. Gong, X. Kang, W. Yao, Multi-fidelity prediction of fluid flow based on transfer learning using Fourier neural operator, *Physics of Fluids* 35 (7) (2023).
- [21] A. Zhou, C. Lorusso, A. Hemmasian, A. B. Farimani, Strategies for Pretraining Neural Operators, *arXiv preprint arXiv:2406.08473* (2024).
- [22] R. Tali, A. Rabeh, C.-H. Yang, M. Shadkhah, S. Karki, A. Upadhyaya, S. Dhakshinamoorthy, M. Saadati, S. Sarkar, A. Krishnamurthy, et al., FlowBench: A Large Scale Benchmark for Flow Simulation over Complex Geometries, *arXiv preprint arXiv:2409.18032* (2024).
- [23] P. Du, M. H. Parikh, X. Fan, X.-Y. Liu, J.-X. Wang, CoNFILD: Conditional Neural Field Latent Diffusion Model Generating Spatiotemporal Turbulence, *arXiv preprint arXiv:2403.05940* (2024).
- [24] H. Gao, S. Kaltenbach, P. Koumoutsakos, Generative Learning for Forecasting the Dynamics of Complex Systems, *arXiv preprint arXiv:2402.17157* (2024).
- [25] H. Wu, H. Luo, H. Wang, J. Wang, M. Long, Transolver: A Fast Transformer Solver for PDEs on General Geometries, *arXiv e-prints* (Feb. 2024).
- [26] Z. Li, D. Shu, A. Barati Farimani, Scalable transformer for pde surrogate modeling, *Advances in Neural Information Processing Systems* 36 (2024).

- [27] M. Lienen, D. Lüdke, J. Hansen-Palmus, S. Günnemann, From zero to turbulence: Generative modeling for 3d flow simulation, arXiv preprint arXiv:2306.01776 (2023).
- [28] Z. Deng, H. Liu, B. Shi, Z. Wang, F. Yu, Z. Liu, G. Chen, Temporal predictions of periodic flows using a mesh transformation and deep learning-based strategy, *Aerospace Science and Technology* 134 (2023) 108081.
- [29] W. Zhong, H. Meidani, Physics-Informed Geometry-Aware Neural Operator, arXiv preprint arXiv:2408.01600 (2024).
- [30] S. Xu, Z. Sun, R. Huang, D. Guo, G. Yang, S. Ju, A practical approach to flow field reconstruction with sparse or incomplete data through physics informed neural network, *Acta Mechanica Sinica* 39 (3) (2023) 322302.
- [31] G. E. Karniadakis, I. G. Kevrekidis, L. Lu, P. Perdikaris, S. Wang, L. Yang, Physics-informed machine learning, *Nature Reviews Physics* 3 (6) (2021) 422–440.
- [32] Z. Zhou, G. He, S. Wang, G. Jin, Subgrid-scale model for large-eddy simulation of isotropic turbulent flows using an artificial neural network, *Computers & Fluids* 195 (2019) 104319.
- [33] X. Yang, S. Zafar, J.-X. Wang, H. Xiao, Predictive large-eddy-simulation wall modeling via physics-informed neural networks, *Physical Review Fluids* 4 (3) (2019) 034602.
- [34] Z. Wang, K. Luo, D. Li, J. Tan, J. Fan, Investigations of data-driven closure for subgrid-scale stress in large-eddy simulation, *Physics of Fluids* 30 (12) (2018).
- [35] R. Maulik, O. San, A. Rasheed, P. Vedula, Data-driven deconvolution for large eddy simulations of Kraichnan turbulence, *Physics of Fluids* 30 (12) (2018) 125109.
- [36] Z. Yuan, Y. Wang, X. Wang, J. Wang, Adjoint-based variational optimal mixed models for large-eddy simulation of turbulence, *Physics of Fluids* 35 (7) (2023).
- [37] M. Raissi, A. Yazdani, G. E. Karniadakis, Hidden fluid mechanics: Learning velocity and pressure fields from flow visualizations, *Science* 367 (6481) (2020) 1026–1030.
- [38] S. Cai, Z. Wang, F. Fuest, Y. J. Jeon, C. Gray, G. E. Karniadakis, Flow over an espresso cup: inferring 3-D velocity and pressure fields from tomographic background oriented Schlieren via physics-informed neural networks, *Journal of Fluid Mechanics* 915 (2021) A102.
- [39] L. Zhu, X. Jiang, A. Lefauve, R. R. Kerswell, P. Linden, New insights into experimental stratified flows obtained through physics-informed neural networks, *Journal of Fluid Mechanics* 981 (2024) R1.
- [40] Z. Zhao, X. Ding, B. A. Prakash, Pinnsformer: A transformer-based framework for physics-informed neural networks, arXiv preprint arXiv:2307.11833 (2023).
- [41] N. Wandel, M. Weinmann, R. Klein, Teaching the incompressible Navier–Stokes equations to fast neural surrogate models in three dimensions, *Physics of Fluids* 33 (4) (2021).
- [42] H. Yang, Z. Li, X. Wang, J. Wang, An Implicit Factorized Transformer with Applications to Fast Prediction of Three-dimensional Turbulence, *Theoretical and Applied Mechanics Letters* (2024) 100527.
- [43] Z. Li, W. Peng, Z. Yuan, J. Wang, Fourier neural operator approach to large eddy simulation of three-dimensional turbulence, *Theoretical and Applied Mechanics Letters* 12 (6) (2022) 100389.
- [44] S. Cuomo, V. S. Di Cola, F. Giampaolo, G. Rozza, M. Raissi, F. Piccialli, Scientific machine learning through physics-informed neural networks: Where we are and what’s next, *Journal of Scientific Computing* 92 (3) (2022) 88.
- [45] S. Cai, Z. Wang, S. Wang, P. Perdikaris, G. E. Karniadakis, Physics-informed neural networks for heat transfer problems, *Journal of Heat Transfer* 143 (6) (2021) 060801.
- [46] S. Cai, Z. Mao, Z. Wang, M. Yin, G. E. Karniadakis, Physics-informed neural networks (PINNs) for fluid mechanics: A review, *Acta Mechanica Sinica* 37 (12) (2021) 1727–1738.
- [47] Y. Wang, Z. Yuan, C. Xie, J. Wang, Artificial neural network-based spatial gradient models for large-eddy simulation of turbulence, *AIP Advances* 11 (5) (2021).
- [48] C. Xie, J. Wang, K. Li, C. Ma, Artificial neural network approach to large-eddy simulation of compressible isotropic turbulence, *Physical Review E* 99 (5) (2019) 053113.
- [49] J. Ling, A. Kurzawski, J. Templeton, Reynolds averaged turbulence modelling using deep neural networks with embedded invariance, *Journal of Fluid Mechanics* 807 (2016) 155–166.
- [50] Z. Yuan, C. Xie, J. Wang, Deconvolutional artificial neural network models for large eddy simulation of turbulence, *Physics of Fluids* 32 (11) (2020).
- [51] V. Parfenyev, M. Blumenau, I. Nikitin, Inferring parameters and reconstruction of two-dimensional turbulent flows with physics-informed neural networks, *JETP Letters* (2024) 1–9.
- [52] C. White, J. Berner, J. Kossaifi, M. Elleithy, D. Pitt, D. Leibovici, Z. Li, K. Azizzadenesheli, A. Anandkumar, Physics-informed neural operators with exact differentiation on arbitrary geometries, in: *The Symbiosis of Deep Learning and Differential Equations III*, 2023.
- [53] Y. Dubief, F. Delcayre, On coherent-vortex identification in turbulence, *Journal of turbulence* 1 (1) (2000) 011.
- [54] J. C. Hunt, A. A. Wray, P. Moin, Eddies, streams, and convergence zones in turbulent flows, *Studying turbulence using numerical simulation databases, 2. Proceedings of the 1988 summer program* (1988).
- [55] M. M. Rogers, R. D. Moser, Direct simulation of a self-similar turbulent mixing layer, *Physics of Fluids* 6 (2) (1994) 903–923.
- [56] X. Wang, J. Wang, S. Chen, Compressibility effects on statistics and coherent structures of compressible turbulent mixing layers, *Journal of Fluid Mechanics* 947 (2022) A38.
- [57] Y. Wang, Z. Yuan, X. Wang, J. Wang, Constant-coefficient spatial gradient models for the sub-grid scale closure in large-eddy simulation of turbulence, *Physics of Fluids* 34 (9) (2022).
- [58] D. Hendrycks, K. Gimpel, Gaussian error linear units (GELUs), arXiv preprint arXiv:1606.08415 (2016).
- [59] P. K. Diederik, Adam: A method for stochastic optimization, (No Title) (2014).
- [60] C. Xie, J. Wang, W. E. Modeling subgrid-scale forces by spatial artificial neural networks in large eddy simulation of turbulence, *Physical Review Fluids* 5 (5) (2020) 054606.
- [61] S. Wang, Y. Teng, P. Perdikaris, Understanding and mitigating gradient flow pathologies in physics-informed neural networks, *SIAM Journal on Scientific Computing* 43 (5) (2021) A3055–A3081.

- [62] P. Moin, K. Squires, W. Cabot, S. Lee, A dynamic subgrid-scale model for compressible turbulence and scalar transport, *Physics of Fluids A: Fluid Dynamics* 3 (11) (1991) 2746–2757.
- [63] P. Sagaut, *Large eddy simulation for incompressible flows: an introduction*, Springer Science & Business Media, 2005.
- [64] C. Meneveau, J. Katz, Scale-invariance and turbulence models for large-eddy simulation, *Annual Review of Fluid Mechanics* 32 (1) (2000) 1–32.
- [65] R. D. Moser, S. W. Haering, G. R. Yalla, Statistical properties of subgrid-scale turbulence models, *Annual Review of Fluid Mechanics* 53 (1) (2021) 255–286.
- [66] O. Reynolds, IV. On the dynamical theory of incompressible viscous fluids and the determination of the criterion, *Philosophical transactions of the royal society of london.(a.)* (186) (1895) 123–164.
- [67] S. Raghu, R. Nayek, V. Chalamalla, Physics Informed Neural Networks for Free Shear Flows, arXiv preprint arXiv:2404.03542 (2024).
- [68] S. Chen, P. Givi, C. Zheng, X. Jia, Physics-enhanced Neural Operator for Simulating Turbulent Transport, arXiv preprint arXiv:2406.04367 (2024).
- [69] W. Peng, S. Qin, S. Yang, J. Wang, X. Liu, L. L. Wang, Fourier neural operator for real-time simulation of 3D dynamic urban microclimate, *Building and Environment* 248 (2024) 111063.
- [70] T. Luo, Z. Li, Z. Yuan, W. Peng, T. Liu, J. Wang, et al., Fourier neural operator for large eddy simulation of compressible Rayleigh-Taylor turbulence, arXiv preprint arXiv:2404.05834 (2024).
- [71] A. Jiao, Q. Yan, J. Harlim, L. Lu, Solving forward and inverse PDE problems on unknown manifolds via physics-informed neural operators, arXiv preprint arXiv:2407.05477 (2024).
- [72] S. G. Rosofsky, H. Al Majed, E. Huerta, Applications of physics informed neural operators, *Machine Learning: Science and Technology* 4 (2) (2023) 025022.
- [73] Z. Lu, Y. Zhou, Y. Zhang, X. Hu, Q. Zhao, X. Hu, A fast general thermal simulation model based on Multi-Branch Physics-Informed deep operator neural network, *Physics of Fluids* 36 (3) (2024).
- [74] K.-M. Na, C.-H. Lee, Physics-informed deep learning approach to solve optimal control problem, in: *AIAA SCITECH 2024 Forum*, 2024, p. 0945.
- [75] Y. Hao, P. C. Di Leoni, O. Marxen, C. Meneveau, G. E. Karniadakis, T. A. Zaki, Instability-wave prediction in hypersonic boundary layers with physics-informed neural operators, *Journal of Computational Science* 73 (2023) 102120.
- [76] S. Wang, H. Wang, P. Perdikaris, Learning the solution operator of parametric partial differential equations with physics-informed DeepONets, *Science advances* 7 (40) (2021).
- [77] Y. Wang, Z. Li, Z. Yuan, W. Peng, T. Liu, J. Wang, Prediction of turbulent channel flow using Fourier neural operator-based machine-learning strategy, *Physical Review Fluids* 9 (8) (2024) 084604.
- [78] W. Peng, Z. Yuan, Z. Li, J. Wang, Linear attention coupled Fourier neural operator for simulation of three-dimensional turbulence, *Physics of Fluids* 35 (1) (2023).
- [79] M. Momenifar, E. Diau, V. Tarokh, A. D. Bragg, Dimension reduced turbulent flow data from deep vector quantisers, *Journal of Turbulence* 23 (4-5) (2022) 232–264.
- [80] A. Tran, A. Mathews, L. Xie, C. S. Ong, Factorized fourier neural operators, arXiv preprint arXiv:2111.13802 (2021).
- [81] J. Guibas, M. Mardani, Z. Li, A. Tao, A. Anandkumar, B. Catanzaro, Adaptive fourier neural operators: Efficient token mixers for transformers, arXiv preprint arXiv:2111.13587 (2021).
- [82] Z. Hao, Z. Wang, H. Su, C. Ying, Y. Dong, S. Liu, Z. Cheng, J. Song, J. Zhu, GNOT: A general neural operator transformer for operator learning, in: *Proceedings of the 40th International Conference on Machine Learning*, 2023, pp. 12556–12569.
- [83] W. Peng, Z. Yuan, J. Wang, Attention-enhanced neural network models for turbulence simulation, *Physics of Fluids* 34 (2) (2022).
- [84] K. He, X. Zhang, S. Ren, J. Sun, Deep residual learning for image recognition, in: *Proceedings of the IEEE conference on computer vision and pattern recognition*, 2016, pp. 770–778.
- [85] R. Wang, K. Kashinath, M. Mustafa, A. Albert, R. Yu, Towards physics-informed deep learning for turbulent flow prediction, in: *Proceedings of the 26th ACM SIGKDD international conference on knowledge discovery & data mining*, 2020, pp. 1457–1466.
- [86] J. Chen, J. Viquerat, E. Hachem, U-net architectures for fast prediction of incompressible laminar flows, arXiv preprint arXiv:1910.13532 (2019).
- [87] N. Kovachki, Z. Li, B. Liu, K. Azizzadenesheli, K. Bhattacharya, A. Stuart, A. Anandkumar, Neural operator: Learning maps between function spaces with applications to pdes, *Journal of Machine Learning Research* 24 (89) (2023) 1–97.
- [88] Y. Chen, D. Wang, D. S. Feng, G. Tian, V. Gupta, R. Cao, M. Wan, S. Chen, Three-dimensional spatiotemporal wind field reconstruction based on LiDAR and multi-scale PINN, *Applied Energy* (2025).
- [89] H. Gao, L. Sun, J.-X. Wang, PhyGeoNet: Physics-informed geometry-adaptive convolutional neural networks for solving parameterized steady-state PDEs on irregular domain, *Journal of Computational Physics* 428 (2021) 110079.
- [90] K. Shukla, A. D. Jagtap, G. E. Karniadakis, Parallel physics-informed neural networks via domain decomposition, *Journal of Computational Physics* 447 (2021) 110683.
- [91] L. Yang, X. Meng, G. E. Karniadakis, B-PINNs: Bayesian physics-informed neural networks for forward and inverse PDE problems with noisy data, *Journal of Computational Physics* 425 (2021) 109913.
- [92] W. Cho, M. Jo, H. Lim, K. Lee, D. Lee, S. Hong, N. Park, Parameterized physics-informed neural networks for parameterized PDEs, arXiv preprint arXiv:2408.09446 (2024).
- [93] M. Raissi, Z. Wang, M. S. Triantafyllou, G. E. Karniadakis, Deep learning of vortex-induced vibrations, *Journal of Fluid Mechanics* 861 (2019) 119–137.
- [94] H. Xu, W. Zhang, Y. Wang, Explore missing flow dynamics by physics-informed deep learning: The parameterized governing systems, *Physics of Fluids* 33 (9) (2021).
- [95] M. Raissi, P. Perdikaris, G. E. Karniadakis, Physics informed deep learning (Part I): Data-driven solutions of nonlinear partial differential equations, arXiv preprint arXiv:1711.10561 (2017).
- [96] M. Raissi, P. Perdikaris, G. E. Karniadakis, Physics Informed Deep Learning (Part II): Data-driven Discovery of Nonlinear Partial Differen-

- tial Equations, arXiv preprint arXiv:1711.10566 (2017).
- [97] M. Raissi, P. Perdikaris, G. E. Karniadakis, Physics-informed neural networks: A deep learning framework for solving forward and inverse problems involving nonlinear partial differential equations, *Journal of Computational physics* 378 (2019) 686–707.
 - [98] J. Sirignano, K. Spiliopoulos, DGM: A deep learning algorithm for solving partial differential equations, *Journal of computational physics* 375 (2018) 1339–1364.
 - [99] B. Lusch, J. N. Kutz, S. L. Brunton, Deep learning for universal linear embeddings of nonlinear dynamics, *Nature communications* 9 (1) (2018) 4950.
 - [100] Y. LeCun, Y. Bengio, G. Hinton, Deep learning, *nature* 521 (7553) (2015) 436–444.
 - [101] J. Park, H. Choi, Toward neural-network-based large eddy simulation: Application to turbulent channel flow, *Journal of Fluid Mechanics* 914 (2021) A16.
 - [102] A. Beck, D. Flad, C.-D. Munz, Deep neural networks for data-driven LES closure models, *Journal of Computational Physics* 398 (2019) 108910.
 - [103] J. Wu, H. Xiao, R. Sun, Q. Wang, Reynolds-averaged Navier–Stokes equations with explicit data-driven Reynolds stress closure can be ill-conditioned, *Journal of Fluid Mechanics* 869 (2019) 553–586.
 - [104] K. Duraisamy, G. Iaccarino, H. Xiao, Turbulence modeling in the age of data, *Annual review of fluid mechanics* 51 (1) (2019) 357–377.
 - [105] S. L. Brunton, B. R. Noack, P. Koumoutsakos, Machine learning for fluid mechanics, *Annual review of fluid mechanics* 52 (1) (2020) 477–508.
 - [106] T. Ishihara, T. Gotoh, Y. Kaneda, Study of high-Reynolds number isotropic turbulence by direct numerical simulation, *Annual review of fluid mechanics* 41 (1) (2009) 165–180.
 - [107] M. Germano, U. Piomelli, P. Moin, W. H. Cabot, A dynamic subgrid-scale eddy viscosity model, *Physics of Fluids A: Fluid Dynamics* 3 (7) (1991) 1760–1765.
 - [108] S. B. Pope, Turbulent flows, *Measurement Science and Technology* 12 (11) (2001) 2020–2021.
 - [109] M. Y. Hussaini, T. A. Zang, Spectral methods in fluid dynamics, Tech. rep. (1986).
 - [110] J. Smagorinsky, General circulation experiments with the primitive equations: I. The basic experiment, *Monthly weather review* 91 (3) (1963) 99–164.
 - [111] Z. Li, H. Zheng, N. Kovachki, D. Jin, H. Chen, B. Liu, K. Azizzadenesheli, A. Anandkumar, Physics-informed neural operator for learning partial differential equations, *ACM/JMS Journal of Data Science* 1 (3) (2024) 1–27.
 - [112] A. G. Baydin, B. A. Pearlmutter, A. A. Radul, J. M. Siskind, Automatic differentiation in machine learning: a survey, *Journal of machine learning research* 18 (153) (2018) 1–43.
 - [113] S. Wang, X. Yu, P. Perdikaris, When and why PINNs fail to train: A neural tangent kernel perspective, *Journal of Computational Physics* 449 (2022) 110768.
 - [114] O. Fuks, H. A. Tchelepi, Limitations of physics informed machine learning for nonlinear two-phase transport in porous media, *Journal of Machine Learning for Modeling and Computing* 1 (1) (2020).
 - [115] X. Jin, S. Cai, H. Li, G. E. Karniadakis, NSFnets (Navier-Stokes flow nets): Physics-informed neural networks for the incompressible Navier-Stokes equations, *Journal of Computational Physics* 426 (2021) 109951.
 - [116] Z. Li, N. Kovachki, K. Azizzadenesheli, B. Liu, K. Bhattacharya, A. Stuart, A. Anandkumar, Fourier neural operator for parametric partial differential equations, arXiv preprint arXiv:2010.08895 (2020).
 - [117] G. Wen, Z. Li, K. Azizzadenesheli, A. Anandkumar, S. M. Benson, U-FNO—An enhanced Fourier neural operator-based deep-learning model for multiphase flow, *Advances in Water Resources* 163 (2022) 104180.
 - [118] H. You, Q. Zhang, C. J. Ross, C.-H. Lee, Y. Yu, Learning deep implicit Fourier neural operators (IFNOs) with applications to heterogeneous material modeling, *Computer Methods in Applied Mechanics and Engineering* 398 (2022) 115296.
 - [119] N. Kovachki, S. Lanthaler, S. Mishra, On universal approximation and error bounds for Fourier neural operators, *Journal of Machine Learning Research* 22 (290) (2021) 1–76.
 - [120] S. Song, T. Mukerji, D. Zhang, Physics-informed multi-grid neural operator: theory and an application to porous flow simulation, *Journal of Computational Physics* (2024) 113438.
 - [121] Z. Li, W. Peng, Z. Yuan, J. Wang, Long-term predictions of turbulence by implicit U-Net enhanced Fourier neural operator, *Physics of Fluids* 35 (7) (2023) 075145.
 - [122] S. Wang, P. Perdikaris, Long-time integration of parametric evolution equations with physics-informed deepnets, *Journal of Computational Physics* 475 (2023) 111855.
 - [123] R. Brecht, D. R. Popovych, A. Bihlo, R. O. Popovych, Improving physics-informed deepnets with hard constraints, arXiv preprint arXiv:2309.07899 (2023).